Mon. Not. R. Astron. Soc. **000**, 1–18 (2014) Printed September 10, 2014 (MN LATEX style file v2.2)

The effects of galaxy shape and rotation on the X-ray haloes of early-type galaxies - II. Numerical simulations

Andrea Negri⋆, Silvia Posacki†, Silvia Pellegrini & Luca Ciotti
Department of Physics and Astronomy, University of Bologna, viale Berti Pichat 6/2, 40127 Bologna, Italy

arXiv:1406.0008v2 [astro-ph.GA] 9 Sep 2014

2014 August 20

ABSTRACT

By means of high resolution 2D hydrodynamical simulations, we study the evolution of the hot ISM for a large set of early-type galaxy models, characterized by various degrees of flattening and internal rotation. The galaxies are described by state-of-the-art axisymmetric two-component models, tailored to reproduce real systems; the dark matter haloes follow the Navarro-Frenk-White or the Einasto profile. The gas is produced by the evolving stars, and heated by Type Ia SNe. We find that, in general, the rotation field of the ISM in rotating galaxies is very similar to that of the stars, with a consequent negligible heating contribution from thermalization of the ordered motions. The relative importance of flattening and rotation in determining the final X-ray luminosity L_X and temperature T_X of the hot haloes is a function of the galactic mass. Flattening and rotation in low mass galaxies favour the establishment of global winds, with the consequent reduction of L_X. In medium-to-high mass galaxies, flattening and rotation are not sufficient to induce global winds, however, in the rotating models the nature of the gas flows is deeply affected by conservation of angular momentum, resulting in a reduction of both L_X and T_X.

Key words: galaxies: elliptical and lenticular, cD – galaxies: ISM – galaxies: kinematics and dynamics – X-rays: galaxies – X-rays: ISM – methods: numerical

1 INTRODUCTION

Early-Type galaxies (ETG) are embedded in hot ($10^6 - 10^7$ K), X-ray emitting gaseous haloes (Fabbiano 1989; O'Sullivan et al. 2001), produced mainly by stellar winds and heated by Type Ia supernovae (SNIa) explosions and by the thermalization of stellar motions. In particular, the thermalization of stellar motions is due to the interaction between the stellar and SNIa ejecta and the pre-existing hot ISM (e.g., Parriott & Bregman 2008). A number of different astrophysical phenomena determine the X-ray properties of the hot ISM, such as stellar population evolution, galaxy structure and internal kinematics, AGN presence, and environmental effects. In particular, one of the empirical discoveries that followed the analysis of first X-ray data of ETGs was the sensitivity of the hot gas content to major galaxy properties as the shape of the mass distribution, and the mean rotation velocity of the stellar component (see Kim & Pellegrini 2012; Mathews & Brighenti 2003 for a full discussion of the most relevant observational and theoretical aspects concerning the X-ray haloes). From *Einstein* observations it was found that on average, at any fixed optical luminosity L_B, rounder systems had larger total X-ray luminosity L_X and L_X/L_B (a measure of the galactic hot gas content), than flatter ETGs and S0 galaxies (Eskridge et al. 1995). Moreover, galaxies with axial ratio close to unity spanned the full range of L_X, while flat systems had $L_X \lesssim 10^{41}$erg s^{-1}. This result was not produced by flat galaxies having a lower L_B with respect to round ETGs, since it held even in the range of L_B where the two shapes coexist (Pellegrini 1999). Moreover it was found that L_X/L_B can be high only in slowly rotating galaxies, and is limited to low values for fast rotating ones (Pellegrini et al. 1997; Sarzi et al. 2010). The relationship between L_X and shape/rotation was reconsidered, confirming the above trends, for the *ROSAT* PSPC sample (Pellegrini 2012), and for the *Chandra* sample (Li et al. 2011; Boroson et al. 2011; Sarzi et al. 2013). In particular, Sarzi et al. (2013), after confirming that slow rotators generally have the largest L_X and L_X/L_B values, also found that their gas temperature T_X values are consistent just with the thermalization of the stellar kinetic energy, estimated from σ_e (the luminosity averaged stellar velocity dispersion within the effective radius R_e). Fast rotators, instead, have generally lower L_X and L_X/L_B values, and the more so the larger their degree of rotational support; the T_X values of fast rotators keep below 0.4 keV and do not scale with σ_e. Therefore, there seems to be a dependence of the hot gas content and temperature on the galactic shape and internal dynamics. The investigation of the origin of this still poorly understood sensitivity is the goal of the present paper.

Theoretically, different possibilities have been proposed, and explored both analytically (Ciotti & Pellegrini 1996, hereafter CP96; Posacki et al. 2013, hereafter P13) and numerically (Brighenti & Mathews 1996; D'Ercole & Ciotti 1998, hereafter DC98; Negri et al.

⋆ E-mail: andrea.negri@unibo.it
† E-mail: silvia.posacki@unibo.it

© 2014 RAS

2014, hereafter N14). The proposed explanations can be classified in two broad categories: the *energetic* ones and the *hydrodynamical* ones. Of course, the difference is not sharp, as the flow energetics affects the hydrodynamical evolution, and different hydrodynamical configurations lead to different redistributions of the energy available.

Explanations based on energetic effects suppose that the ISM in flat and rotating galaxies is less bound than in more round and non rotating galaxies of similar luminosity (and so of similar SNIa energy input), so that in the former objects the ISM is more prone to develop a global/partial galactic wind, with the consequent decrease of $L_{\rm X}$. A subdivision of energetic explanations is represented by consideration of *flattening* effects vs. *rotational* effects. The flattening explanation requires that flat galaxies have shallower potential wells than rounder galaxies of similar luminosity, so the gas is less bound (independently of the galaxy kinematical support, ordered rotation or velocity dispersion). In this scenario, the X-ray under-luminosity of rotating galaxies is just a by-product of the fact that fast rotation can be associated only to significant flattening. The rotational explanation, instead, assumes that the gas injected in the galaxy retains the stellar streaming motion, and so it is less bound in rotating galaxies than in velocity dispersion supported galaxies of similar shape: the correlation of X-ray under-luminosity with galaxy flattening is now a by-product of the fact that rotating galaxies are generally flat. Note that in this explanation the thermalization of ordered ISM velocities is low, and then the ISM also lacks the corresponding energetic input; so the two effects (lower effective binding energy but also lower heating) are in competition. Indeed, the stellar random kinetic energy is always supplied to the ISM, while the thermalization of the ordered kinetic energy depends on the relative motion between the stellar population and the ISM (see also Pellegrini 2011, P13). P13 proposed that a lower energy injection at fixed $L_{\rm B}$, due to the lack of thermalization of stellar streaming motions, could explain the lower $T_{\rm X}$ of rotating galaxies. The energetic scenario has been explored analytically in CP96 by using two-component Miyamoto-Nagai models, and in P13 by building a wide set of more realistic ETG models, with different flattened structures and kinematics. These works showed that the binding energy of the gas depends on the procedure adopted to "flatten" the galaxy models, and that rotation affects also the hot gas temperature. Preliminary numerical results for S0 galaxies suggest a low thermalization in rotating systems (N14).

Explanations based on hydrodynamical effects are less direct. In this scenario the rotation of the gas injected in the galaxy leads to hydrodynamical configurations of the ISM that, for different but cooperating reasons associated with angular momentum conservation, are less X-ray luminous than in non rotating systems. For example, the gas density in the central galactic region is lower in rotating models, where a rotationally supported cold disc forms, than in non-rotating ones, where the gas flows straight to the centre, forming a hot, dense core. Thus, the X-ray faintness is not due to the onset of galactic winds, but to redistribution of the gas inside the galaxy. Now rotation is the main driver of X-ray under luminosity, and correlation with galaxy flattening is a by-product. Exploratory numerical simulations (N14) further showed that the X-ray under-luminosity of flat objects could be due to hydrodynamical effects associated with angular momentum conservation of gas injected at large radii for massive galaxies, but it is more and more due to energetic reasons for low-mass systems.

Empirically, due to the difficulty to observationally disentangle purely rotational and purely flattening effects, it is not easy to draw a clear cut between the two broad explanations illustrated above. First of all, since rotation is dependent on flattening, only galaxies sufficiently flattened are expected to rotate significantly. Secondly, given that the observed flattening in real objects is affected by projection effects, intrinsically flattened galaxies, if observed face-on, can be found in the region occupied by rounder galaxies in the ellipticity-X-ray properties diagrams.

For these reasons, by using high-resolution 2D hydrodynamical simulations of gas flows in realistic, state-of-the-art models of ETGs, we study this long-standing issue of the X-ray under-luminosity of flat and rotating galaxies, together with the properties of their $T_{\rm X}$ values. In order to derive robust conclusions, we perform a large-scale exploration of the parameter space of realistic (axisymmetric) galaxy models characterized by different stellar mass, intrinsic flattening, distribution of dark matter, and internal kinematics. In particular, the galaxy flattening is supported by ordered rotation (isotropic rotators) or by tangential anisotropy. All galaxy models are constructed by using the Jeans code described in P13, and are tailored to reproduce the observed properties and scaling laws of ETGs. These simulations also allow to test how much simple energetic estimates (such those of CP96 and P13) can be trustworthy in interpreting the global properties of the hot gaseous X-ray coronae.

The paper is organized as follows. In Section 2 we describe the main ingredients of the simulations, such as the galaxy models and the input physics. The main results are presented in Section 3, and Section 4 summarizes the conclusions.

2 THE SIMULATIONS

2.1 The galaxy models

For the simulations we adopt axisymmetric two-component galaxy models, where the stellar component can have different intrinsic flattening, while for simplicity the DM halo is kept spherical. In particular, the stellar component is described by the deprojection (Mellier & Mathez 1987) of the de Vaucouleurs (1948) law, generalized for ellipsoidal axisymmetric distributions,

$$\rho_*(R,z) = \rho_0 \xi^{-0.855} \exp(-\xi^{1/4}), \tag{1}$$

with

$$\rho_0 = \frac{M_* b^{12}}{16\pi q R_{\rm e0}^3 \Gamma(8.58)}, \quad \xi = \frac{b^4}{R_{\rm e0}} \sqrt{R^2 + \frac{z^2}{q^2}}, \tag{2}$$

where (R,φ,z) are the cylindrical coordinates and $b \simeq 7.67$. The flattening is controlled by the parameter $q \leqslant 1$, so that the minor axis is aligned with the z axis. $R_{\rm e0}$ is the projected half mass radius (effective radius) when the galaxy is seen face-on; for an edge-on view, the circularized effective radius is $R_{\rm e} = R_{\rm e0}\sqrt{q}$. In the simulations we restrict to q values of (1, 0.6, 0.3), corresponding to E0, E4 and E7 galaxies when seen edge-on. For the DM halo we adopt the NFW (Navarro et al. 1997) or the Einasto (1965) profiles.

All models belong to two different *sets*, defined by the specific profile of the DM halo. The first set is characterized by an untruncated NFW profile

$$\rho_{\rm h}(r) = \frac{\rho_{\rm crit}\, \delta_{\rm c} r_{\rm h}}{r(1+r/r_{\rm h})^2}, \tag{3}$$

where $\rho_{\rm crit} = 3H^2/8\pi G$ is the critical density for closure. We refer to the DM mass enclosed within r_{200} (the radius of a sphere of mean interior density $200\,\rho_{\rm crit}$), as to the halo mass $M_{\rm h}$. Following Navarro et al. (1997)

$$\delta_{\rm c} = \frac{200}{3} \frac{c^3}{\ln(1+c) - c/(1+c)}, \quad c \equiv \frac{r_{200}}{r_{\rm h}}. \tag{4}$$

Table 1. Fundamental galaxy parameters for the NFW and Einasto sets of models.

Name	$L_{\rm B}$	$R_{\rm e}$	M_*	$M_{\rm h}$	$\sigma_{\rm e8}^{\rm NFW}$	$\sigma_{\rm e8}^{\rm EIN}$	$f_{\rm DM}^{\rm NFW}$	$f_{\rm DM}^{\rm EIN}$	c
	$(10^{11}L_{\rm B\odot})$	(kpc)	$(10^{11}M_\odot)$	$(10^{11}M_\odot)$	(km s^{-1})	(km s^{-1})			
(1)	(2)	(3)	(4)	(5)	(6)	(7)	(8)	(9)	(10)
$E0^{200}$	0.27	4.09	1.25	25	200	200	0.61	0.57	37
$EO4^{200}_{IS}$	0.27	4.09	1.25	25	166	166	0.63	0.59	37
$EO4^{200}_{VD}$	0.27	4.09	1.25	25	179	179	0.63	0.59	37
$EO7^{200}_{IS}$	0.27	4.09	1.25	25	124	124	0.66	0.62	37
$EO7^{200}_{VD}$	0.27	4.09	1.25	25	148	149	0.66	0.62	37
$FO4^{200}_{IS}$	0.27	4.09	1.25	25	178	179	0.59	0.55	37
$FO4^{200}_{VD}$	0.27	4.09	1.25	25	191	192	0.59	0.55	37
$FO7^{200}_{IS}$	0.27	4.09	1.25	25	150	151	0.57	0.53	37
$FO7^{200}_{VD}$	0.27	4.09	1.25	25	178	179	0.57	0.53	37
$E0^{250}$	0.65	7.04	3.35	67	250	250	0.59	0.55	28
$EO4^{250}_{IS}$	0.65	7.04	3.35	67	207	208	0.62	0.57	28
$EO4^{250}_{VD}$	0.65	7.04	3.35	67	223	224	0.62	0.57	28
$EO7^{250}_{IS}$	0.65	7.04	3.35	67	154	155	0.66	0.61	28
$EO7^{250}_{VD}$	0.65	7.04	3.35	67	184	185	0.66	0.61	28
$FO4^{250}_{IS}$	0.65	7.04	3.35	67	223	224	0.57	0.53	28
$FO4^{250}_{VD}$	0.65	7.04	3.35	67	240	241	0.57	0.53	28
$FO7^{250}_{IS}$	0.65	7.04	3.35	67	189	190	0.56	0.51	28
$FO7^{250}_{VD}$	0.65	7.04	3.35	67	223	224	0.56	0.51	28
$E0^{300}$	1.38	11.79	7.80	160	300	300	0.62	0.57	22
$EO4^{300}_{IS}$	1.38	11.79	7.80	160	248	249	0.64	0.60	22
$EO4^{300}_{VD}$	1.38	11.79	7.80	160	267	269	0.64	0.60	22
$EO7^{300}_{IS}$	1.38	11.79	7.80	160	185	185	0.68	0.64	22
$EO7^{300}_{VD}$	1.38	11.79	7.80	160	221	223	0.68	0.64	22
$FO4^{300}_{IS}$	1.38	11.79	7.80	160	266	268	0.60	0.55	22
$FO4^{300}_{VD}$	1.38	11.79	7.80	160	286	288	0.60	0.55	22
$FO7^{300}_{IS}$	1.38	11.79	7.80	160	224	225	0.59	0.54	22
$FO7^{300}_{VD}$	1.38	11.79	7.80	160	265	267	0.59	0.54	22

Notes: (1) Model name: E0 identifies the spherical progenitor, and the superscript is the value of $\sigma_{\rm e8}$. For the other models, the nomenclature is as follows: for example, $FO4^{200}_{IS}$ means a face-on flattened E4 galaxy, obtained from the $E0^{200}$ progenitor, with isotropic rotation. (2) Luminosities in the *B* band. (3) Effective radius (for a FO view for FO-built models, and an EO view for EO-built models). For FO-built models, the edge-on effective radius is reduced by a factor $\sqrt{q}$ (Sect. 2.1). (4) Total stellar mass. (5) Total DM mass. (6) – (7) Stellar velocity dispersion, as the luminosity-weighted average within a circular aperture of radius $R_{\rm e}/8$, for the NFW and Einasto sets, respectively; for non-spherical models, $\sigma_{\rm e8}$ is the edge-on viewed value. (8) – (9) DM fraction enclosed within a sphere of radius $R_{\rm e}$ for the NFW and Einasto sets, respectively. (10) Concentration parameter for the NFW set.

The models in the second set are embedded in an Einasto profile

$$\rho_{\rm h}(r) = \rho_{\rm c} e^{d_n - x}, \quad x \equiv d_n \left(\frac{r}{r_{\rm h}}\right)^{1/n} \tag{5}$$

where $\rho_{\rm c}$ is the density at the spatial half-mass radius $r_{\rm h}$, n is a free parameter, and

$$d_n \simeq 3n - \frac{1}{3} + \frac{8}{1215n} \tag{6}$$

(Retana-Montenegro et al. 2012). The total gravitational field is computed by using the code described in P13, and the same code is also used to solve numerically the Jeans equations for the velocity fields of the stars, under the implicit assumption of a two-integral distribution function. Ordered and random motions in the azimuthal direction are described using the Satoh (1980) k-decomposition. Following P13, the model parameters are tuned to reproduce the Faber–Jackson and the size–luminosity relations as given by Desroches et al. (2007) for $\approx 10^5$ ETGs in the SDSS; the stellar mass-to-light ratios adopted pertain to a 12 Gyr old stellar population with a Kroupa initial mass function (Maraston 2005).

In each of the two sets, we consider different *families* of models, built following the procedure described in P13 (Sects. 3.3 and

3.4). Here we just recall the main steps. Each family is associated with a spherical galaxy, that we call the "progenitor". The progenitor structural parameters are determined by assigning σ_{e8} (the aperture luminosity-weighted velocity dispersion within $R_e/8$), and then deriving the luminosity and effective radius R_e of the galaxy from the scaling laws cited above. Then, from a chosen stellar mass-to-light ratio, the stellar mass M_* is derived. Finally, the parameters of the DM halo are determined in order to reproduce the assumed σ_{e8} and fixing $M_h/M_* \simeq 20$ (Behroozi et al. 2013). In the NFW set, these constraints produce $r_h \simeq 2R_e$, $22 \lesssim c \lesssim 37$, and a DM fraction f_{DM} within a sphere of radius R_e of $\simeq 0.6$ for the spherical progenitors. For the Einasto set we fix $n = 6$, and we find that $r_h \simeq 20R_e$, and $f_{DM} \simeq 0.56$ for the spherical progenitor.

In each of the two sets we considered three values of σ_{e8} for the spherical progenitors, i.e., 200, 250 and 300 km s^{-1}. Therefore, each of the two sets is made of 3 families of models, for a total of 6 spherical progenitors. Table 1 lists all the relevant parameters characterizing the progenitors galaxy models for both sets. The flattened descendants of each progenitor with intrinsic flattening of E4 ($q = 0.6$) and E7 ($q = 0.3$), are derived as follows. We produce two flattened models for each value of q. The first flattened model is called "face-on built" (hereafter FO-built), since, when observed face-on, its R_e is the same as that of the spherical progenitor; this requires FO-built flattened models to be more and more concentrated as q decreases ($\rho_* \propto q^{-1}$). The second flattened model instead, when seen edge-on, has the same circularized R_e of the spherical progenitor, thus we call it "edge-on built" (hereafter EO-built); this property makes the EO-built models expand with decreasing q ($\rho_* \propto \sqrt{q}$). Therefore, a spherical progenitor with a given value of σ_{e8} produces four flat galaxies: two E4 models (FO and EO built), and two E7 models (FO and EO built). As a further step, in order to study the effects of galaxy rotation, we assume two kinematical supports for each flattened system: one corresponding to a velocity dispersion supported galaxy (VD models), and the other one to an isotropic rotator (IS models). These two configurations are obtained by setting the Satoh parameter k equal to 0 and 1, respectively (see P13, eqs. B3 and B4). In the flattening procedure the DM halo is maintained fixed to that of the progenitor. Note that our flattened models are representative of ETGs since they are consistent with their observed properties. We indeed checked for models lying outside the observed scatter of the scaling laws, but our adopted flattening procedure is quite robust in producing acceptable models, so that we retained all of them.

Summarizing, from each spherical progenitor of given σ_{e8}, eight flattened models are obtained (see Tab. 1), and we refer to this group of nine galaxy models as to a family. All models belonging to a family can be identified either by the σ_{e8} value of the spherical progenitor, or by their stellar mass M_* (or B luminosity), or DM halo mass; note however that while these last three quantities are kept constant within a family, the σ_{e8} of the descendants varies. Indeed, the modification of stellar structure involves a change in the stellar kinematics, and so in the value of σ_{e8}; in particular, for our models σ_{e8} decreases for increasing flattening (see P13 for a comprehensive discussion). Note that σ_{e8} depends on the line-of-sight direction for non-spherical models; when quoting σ_{e8} for the latter models, in the following, we refer to the edge-on projection.

2.2 Hydrodynamical equations

The input physics is fully described in DC98 and N14; here we just summarize the main ingredients. We account for mass sources due to stellar mass losses and SNIa ejecta, momentum injections due to the azimuthal streaming motion of the stellar population, and energy sources due to the thermalization of stellar motions and SNIa explosions. Star formation and feedback from a central black hole are not considered. The corresponding equations are

$$\frac{\partial \rho}{\partial t} + \nabla \cdot (\rho \boldsymbol{u}) = \dot\rho_{SN} + \dot\rho_* \equiv \dot\rho, \tag{7}$$

$$\rho \frac{\partial \boldsymbol{u}}{\partial t} + \rho\,(\boldsymbol{u}\cdot\nabla)\,\boldsymbol{u} = -\nabla p - \rho \nabla \Phi_{tot} + \dot\rho\,(\boldsymbol{v} - \boldsymbol{u}), \tag{8}$$

$$\begin{aligned}\frac{\partial E}{\partial t} + \nabla \cdot (E\boldsymbol{u}) = &-p\nabla\cdot\boldsymbol{u} - \mathscr{L} + \dot\rho_{SN}\frac{u_s^2}{2} \\ &+ \frac{\dot\rho}{2}\left[\|\boldsymbol{v}-\boldsymbol{u}\|^2 + \mathrm{Tr}(\boldsymbol{\sigma}^2)\right],\end{aligned} \tag{9}$$

where ρ, $\boldsymbol{u}$, E, p, Φ_{tot}, $\mathscr{L}$, u_s, $\boldsymbol{v} = v_\varphi \mathbf{e}_\varphi$ and $\boldsymbol{\sigma}^2$ are respectively the ISM mass density, velocity, internal energy density, pressure, total gravitational potential, bolometric radiative losses per unit time and volume, the velocity of the SNIa ejecta ($u_s \simeq 8.5 \times 10^3$ km s^{-1}, corresponding to 10^{51} erg associated with an ejecta of 1.4 $M_\odot$), the streaming velocity and the velocity dispersion tensor of the stellar component. The ISM is considered as a fully ionized monoatomic gas, with $p = (\gamma - 1)E$, $\gamma = 5/3$, and $\mu \simeq 0.62$; as usual the gas self-gravity is neglected.

The total mass injection rate per unit volume $\dot\rho$ has a contribution from SNIa events $\dot\rho_{SN} = \alpha_{SN}(t)\rho_*$ and from stellar winds $\dot\rho_* = \alpha_*(t)\rho_*$, where

$$\alpha_{SN}(t) = \frac{1.4 M_\odot}{M_*} R_{SN}(t), \quad \alpha_*(t) = 3.3 \times 10^{-12} t_{12}^{-1.3}\ (\mathrm{yr}^{-1}). \tag{10}$$

The SNIa explosion rate $R_{SN}(t)$ is given by

$$R_{SN}(t) = 0.16\, h^2 \times 10^{-12} L_B\, t_{12}^{-s}\ (\mathrm{yr}^{-1}), \tag{11}$$

where $h = H_0/70\,\mathrm{km\,s^{-1}\,Mpc^{-1}}$, L_B is the present epoch B-band galaxy luminosity in blue solar luminosities, t_{12} is the age of the stellar population in units of 12 Gyr, and s parametrizes the past evolution. The SNIa's heating rate $L_{SN}(t)$ is obtained from Eq. (11) by assuming that each SNIa event releases 10^{51} erg, and we adopt $s = 1$ in Eq. (11). Since the volume integrated energy and mass injections are dominated by L_{SN} and stellar mass losses, respectively, this choice of s produces a secular time-increase of the specific heating $L_{SN}/\dot\rho$ of the input mass, due to the different time dependence of the mass and energy inputs (e.g., Pellegrini 2012).

The radiative cooling is implemented by adopting a modified version of the cooling law reported in Sazonov et al. (2005), with the lower limit for the ISM temperature of $T = 10^4$ K (see N14 for more details). We also calculate the X-ray emission in the 0.3–8 keV *Chandra* band, and the X-ray emission weighted temperature as

$$L_X = \int \varepsilon_X dV, \quad T_X = \frac{\int T\varepsilon_X dV}{L_X}, \tag{12}$$

respectively, where ε_X is the thermal emissivity in the energy range 0.3–8 keV of a hot, collisionally ionized plasma, obtained by the spectral fitting package XSPEC[1] (spectral model APEC, Smith et al. 2001), and the volume integrals are performed over the whole computational mesh.

As in N14 all the simulations are performed with the ZEUS-MP2 code in cylindrical coordinates, in order to better and uniformly resolve the galaxy equatorial region. The adopted 2D axisymmetric (R, z) grid is organized in 480×960 logarithmically spaced points, extending out to $\simeq$ 100 kpc, with a resolution of $\simeq$ 90 pc in the

[1] http://heasarc.nasa.gov/xanadu/xspec/.

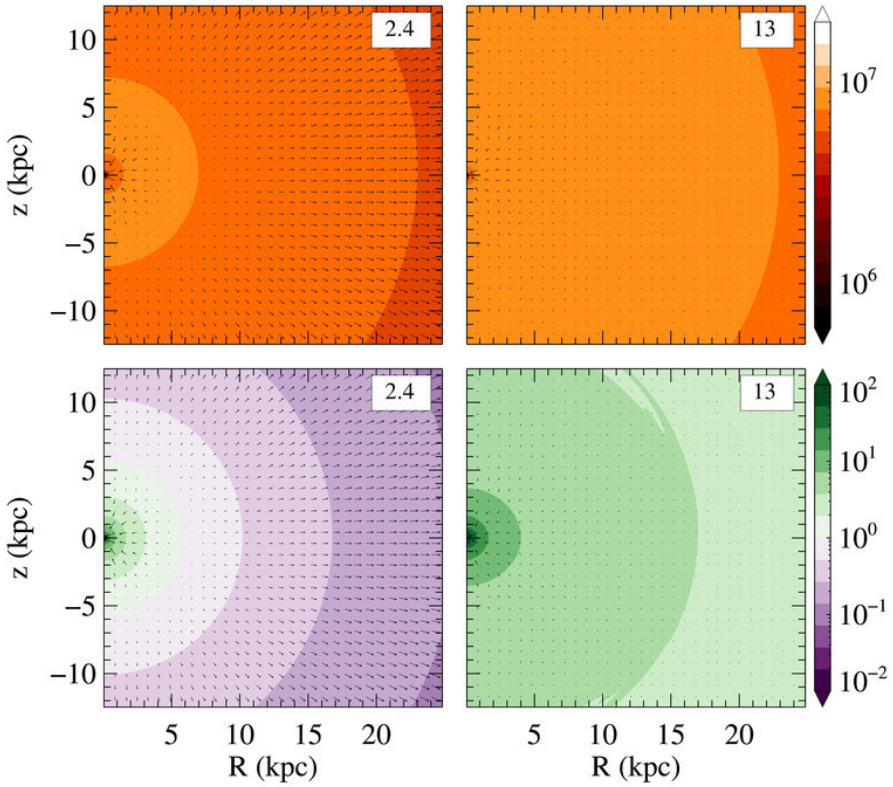

Figure 1. Meridional section of temperature (in K, top panels) and heating over cooling time ratio $t_{\rm heat}/t_{\rm cool}$ (bottom panels), for the E0^{250} model with NFW halo (Table 1), at the times specified in the boxes (in Gyr). We define $t_{\rm cool} = E/\mathscr{L}$ and $t_{\rm heat}$ as the ratio between E and the source terms in the r.h.s of Eq. (9). In the bottom plots, green regions refer to cooling gas, while purple indicate heating dominated regions, as indicated by the colour scale. Arrows show the meridional velocity field, with the longest arrows corresponding to 127 km s^{-1}.

central 10 kpc. We assume that at the beginning of the simulation each galaxy is 2 Gyr old and is depleted of gas due to the feedback of the stellar population; the evolution is followed for 11 Gyr, until an age of 13 Gyr.

2.3 The contribution of stellar kinematics to the ISM energetics

The main issue investigated in this paper is the effect of flattening and ordered rotation on the X ray luminosity and temperature of the ISM. Analytical studies, based on the global energetics arguments, showed that different and competitive effects should be taken into account (CP96, Pellegrini 2011, P13). Some of the expectations have been confirmed by past numerical studies, even though the galaxy models adopted were not tailored on realistic elliptical galaxies, but more on S0/Sa (DC98, N14). In any case, such studies showed that different physical phenomena can be important as a function of the galaxy mass and potential well depth (i.e., whether the ISM is outflowing or inflowing).

In order to compare the results of the numerical simulations with the global energetic estimates, the following quantities are also computed by the hydrodynamical code. The first is the thermalization of stellar random motions, providing an energy input per unit time to the ISM of

$$L_\sigma \equiv \frac{1}{2}\int \dot\rho\, {\rm Tr}(\boldsymbol{\sigma}^2)\, {\rm d}V. \tag{13}$$

Note that while the contribution from stellar random motions is fully independent of the ISM velocity field (see Eq. (8)), the thermalization of the stellar ordered (streaming) motion depends on the relative motion between stars ($\boldsymbol{v}$) and ISM ($\boldsymbol{u}$)

$$\begin{aligned} L_{\rm v} &\equiv \frac{1}{2}\int \dot\rho\, \|\boldsymbol{v}-\boldsymbol{u}\|^2\ {\rm d}V \\ &= \frac{1}{2}\int \dot\rho (u_R^2+u_z^2)\, {\rm d}V + \frac{1}{2}\int \dot\rho (v_\varphi - u_\varphi)^2\, {\rm d}V = L_{\rm m} + L_\varphi, \end{aligned} \tag{14}$$

so that, at variance with L_σ, it cannot be predicted a priori from the knowledge of the galaxy structure and kinematics. Note that in our galaxy models $\boldsymbol{v} = v_\varphi \mathbf{e}_\varphi$, and $L_{\rm m}$ and L_φ are respectively the energy input rate due to the ISM velocity in the meridional plane (R, z), and to the *relative* velocity of stars and the ISM in the azimuthal direction.

As in P13 and N14, we parametrize the thermalized fraction of the available kinetic energy due to stellar streaming with

$$\gamma_{\rm th} \equiv \frac{L_{\rm v}}{L_{\rm rot}}, \tag{15}$$

where

$$L_{\rm rot} \equiv \frac{1}{2}\int \dot\rho\ \|\boldsymbol{v}\|^2\ {\rm d}V \tag{16}$$

is the energy input per unit time that would be injected in a galaxy with an ISM at rest (i.e., $\boldsymbol{u} = 0$), due to thermalization stellar streaming motions. Note that $\gamma_{\rm th}$ is undefined (formally, it diverges) for VD supported models, and can be very large for slow rotators and/or for gas flows with large velocities in the meridional plane (as in the case of galactic winds). Using these definitions, the total energy supplied to the ISM due to stellar motions can be written as

$$L_{\rm kin} \equiv L_\sigma + L_{\rm v} = L_\sigma + \gamma_{\rm th} L_{\rm rot}. \tag{17}$$

Finally, all the luminosities defined above can be converted into equivalent temperatures as

$$T_\sigma = \frac{\mu m_{\rm p}}{3k_{\rm B}M_*}\int \rho_* {\rm Tr}(\boldsymbol{\sigma}^2)\,{\rm d}V, \quad T_{\rm rot} = \frac{\mu m_{\rm p}}{3k_{\rm B}M_*}\int \rho_* \|\boldsymbol{v}\|^2\,{\rm d}V, \tag{18}$$

where $k_{\rm B}$ is the Boltzmann constant and $m_{\rm p}$ is the proton mass, so that

$$T_{\rm kin} = T_\sigma + \gamma_{\rm th}T_{\rm rot}; \quad \gamma_{\rm th}T_{\rm rot} = T_{\rm m} + T_\varphi. \tag{19}$$

3 RESULTS

Here we present the main results of the simulations, focussing on the hydrodynamical evolution of a few representative models, and then on the global properties $L_{\rm X}$ and $T_{\rm X}$ for the two sets of models.

3.1 Hydrodynamics

For illustrative purpose, we present the hydrodynamical evolution of some selected EO-built models belonging to the NFW set. In particular, in the family derived from the E0 progenitor with $\sigma_{\rm e8} = 250$ km s^{-1} (Sect. 3.1.1), we consider the velocity dispersion supported E7 model (Sect. 3.1.2), and the corresponding E7 isotropic rotator (Sect. 3.1.3). In Sect. 3.1.4 we summarize the main similarities and differences with the other models, as well as some considerations on the behaviour of the thermalization parameter $\gamma_{\rm th}$.

In general, as found in N14, the gas flows are found to evolve through two well defined hydrodynamical phases. At the beginning, all the ISM quantities (density, internal energy and velocity) are nearly symmetric with respect to the galactic equatorial plane. During the evolution, the velocity fields become more and more structured, until, after a certain time that depends on the specific model, the reflection symmetry is lost, and it is never restored.

3.1.1 The E0^{250} progenitor

The initial ($t = 2.4$ Gyr) and final ($t = 13$ Gyr) configurations of the ISM are shown in Fig. 1, where we show the meridional section of the ISM temperature (top panels), and the ratio of the heating and cooling time $t_{\rm heat}/t_{\rm cool}$ (bottom panels; green corresponds to a cooling dominated region while violet refers to a heating region). The arrows show the meridional velocity field.

All the ISM physical quantities are stratified on a spherical shape, as a consequence of the galaxy spherical symmetry. A decoupled flow is soon established ($t \simeq 2.4$ Gyr), with an inflow in a round central region surrounded by an outflowing atmosphere. At the same time cold gas accumulates into the centre, due to the lack of rotational support. Starting from the time of decoupling, the evolution appears to be nearly stationary.

The evolution of the ISM temperature reflects the flow evolution: an hot atmosphere approximately isothermal ($T \simeq 5\times10^6$ K) forms at the beginning, containing a cooling region of radius $\simeq 5$ kpc that leads to the formation of a cold core at the very centre (see the green region in the bottom panels). At the end of the simulation, a total of $\simeq 2.6\times10^{10}M_\odot$ of gas are cooled at the centre, while $\simeq 5\times10^9 M_\odot$ have been ejected as a galactic outflow. Overall, $L_{\rm X}$ and $T_{\rm X}$ of this model do not present significant fluctuations (Fig. 2, solid green line), with $L_{\rm X}$ steadily decreasing and $T_{\rm X}$ steadily increasing in pace with the time evolution of mass sources and specific heating.

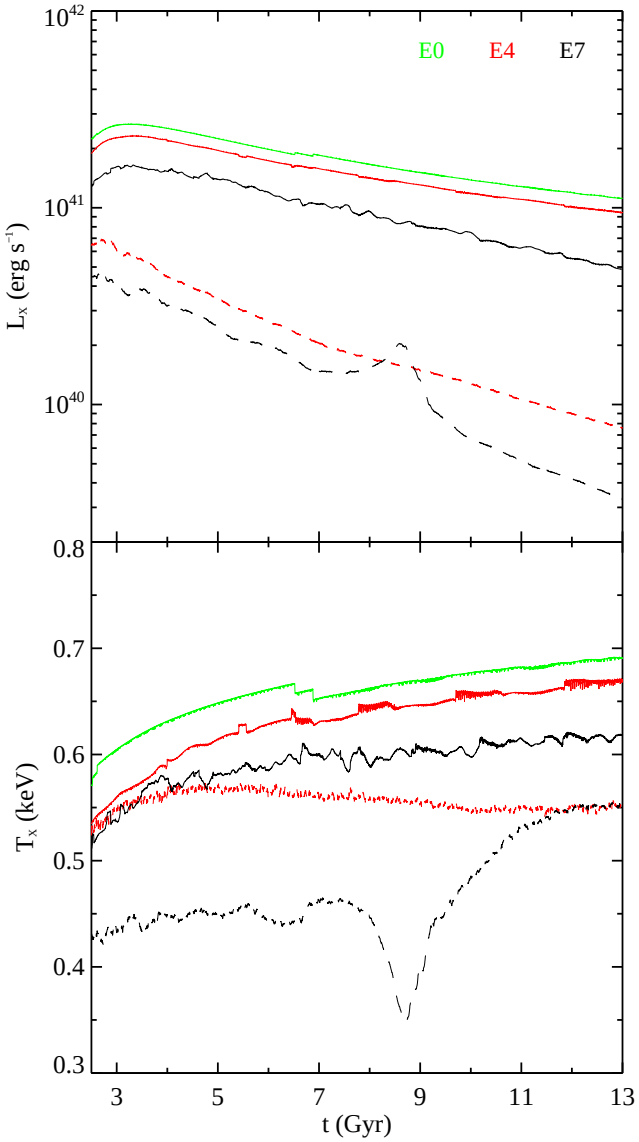

Figure 2. Time evolution of the X-ray luminosity $L_{\rm X}$ and X-ray emission weighted temperature $T_{\rm X}$ for the family derived from the E0^{250} model with the NFW halo. The red and black lines report the evolution of the VD models (solid), and of the IS models (dashed). The colours map the flattening: green, red and black correspond to the E0, E4 and E7 galaxies, respectively.

3.1.2 The EO7$^{250}_{\rm VD}$ galaxy

The ISM evolution of the velocity dispersion supported EO7$^{250}_{\rm VD}$ model presents important similarities with the spherical progenitor. This is not surprising, due to the absence of angular momentum, and to the fact that in general the gravitational potential is much rounder than the associated stellar density distribution (in addition, recall that the DM halo is kept spherical). Therefore, the only major differences between the E0^{250} progenitor and the EO7$^{250}_{\rm VD}$ model are the different spatial regions where the gas is injected, and the different velocity dispersion field of the stars. A direct comparison of the evolution of the two models can be obtained by inspection of Fig. 3, analogous of Fig. 1. At early times the flow is kinematically decoupled, with an equatorial outflow due to the concentrated heating on the equatorial plane (purple region), associated with a polar accretion along the z-axis, evidenced by the green cooling region. As in the spherical

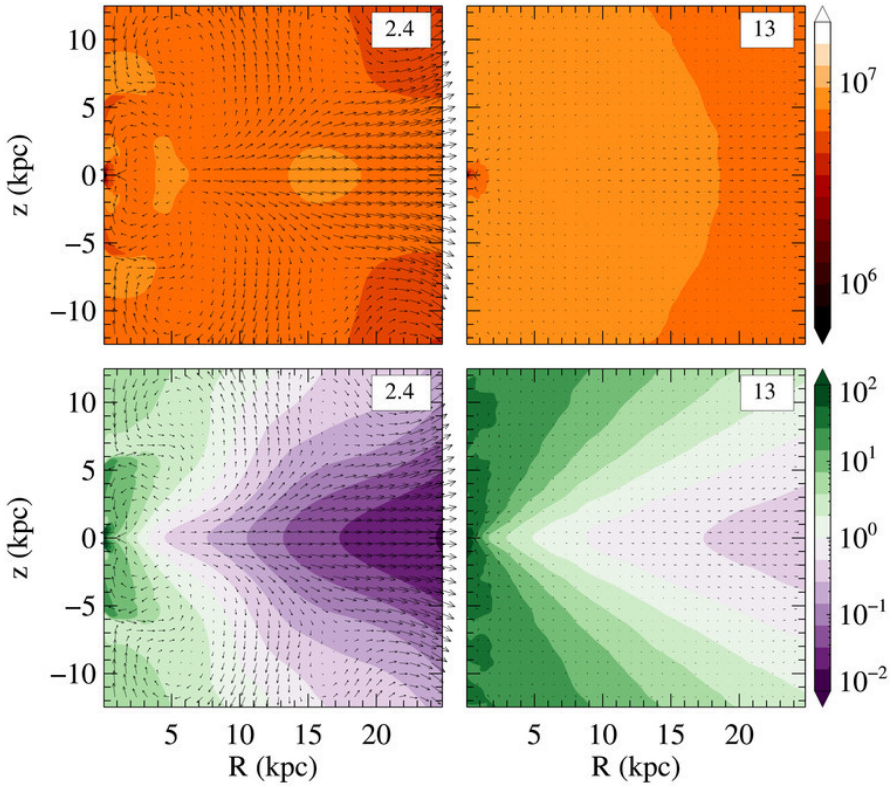

Figure 3. Meridional sections of the temperature (top panels) and heating over cooling time ratio (bottom panels) for the $EO7^{250}_{VD}$ model of the NFW set, at the times specified in the boxes (in Gyr). Arrows are normalized to the same velocity as in Fig. 1.

progenitor, due to the lack of centrifugal support, the cooling material falls directly towards the galaxy centre, where a dense, cold core is formed during the first hundred of Myr. The early flow evolution is characterised by equatorial symmetry and large scale meridional vortexes. The symmetry is lost at $t \simeq 3$ Gyr, followed by a secular decrease of the velocity field. The flow velocities are larger that in the E0 progenitor, due to the weaker gravitational field (consequence of the edge-on flattening). The evolution of L_X and T_X are shown in Fig. 2 (black solid line). Compared to the E0 progenitor, the $EO7^{250}_{VD}$ model has a fainter L_X and a lower T_X, but a similar lack of significant fluctuations in L_X and T_X. At the end of the simulation, the cooled gas at the centre for this model is $\simeq 1.8 \times 10^{10} M_\odot$, while the ejected ISM is $\simeq 7 \times 10^9 M_\odot$. If this model is allowed to have the accretion physics activated for the central black hole, we expect to recover the complex AGN feedback phenomena described elsewhere (Ciotti & Ostriker 2012), with significant reduction of the central accreted mass.

3.1.3 The $EO7^{250}_{IS}$ galaxy

Previous explorations (DC98, N14) revealed that the evolution of gas flows in galaxies with significant ordered rotation of the stellar component is more complex than in velocity dispersion supported systems of similar structure. This is confirmed by the present study. The flow evolution of the $EO7^{250}_{IS}$ is shown in Fig. 4 (where more panels than the previous two models are shown, to better illustrate the more structured evolution of the ISM).

The first major difference of the present model with respect to its VD counterpart is the formation, due to angular momentum conservation, of a rotationally supported, thin and dense cold disc, with a size of $\simeq 5$ kpc. The cold disc grows during galaxy evolution, reaching a final size of $\simeq 10$ kpc. A hot and rarefied zone that secularly increases in size surrounds the cold disc. At early times ($t \simeq 2.1$ Gyr), the ISM in the central regions cools and collapses, producing a low-density region that cannot be replenished by the inflowing gas, which is supported by angular momentum. As time increases, the combination of the centrifugal barrier, that keeps the centre at low density, and the secular increase of the specific heating produce the growth of the heating region (purple zone in Fig. 4, roughly extending as the cold thin disc). We stress that the time and spatial evolution of the t_{heat}/t_{cool} ratio is more affected by cooling time variations than by the secular decrease of the heating time. Being the cooling time very sensitive to the ISM density, t_{heat}/t_{cool} is strongly related to the density distribution evolution.

Another important difference between $EO7^{250}_{IS}$ and $EO7^{250}_{VD}$ concerns the ISM kinematics outside the equatorial plane. As apparent in Fig. 4, starting from $t \simeq 8$ Gyr the meridional velocity field develops a very complex pattern of vortexes above and below the equatorial plane. This behaviour is associated with the formation of a large cooling region (in green), and corresponds respectively to a peak and a drop in the evolution of L_X and T_X (Fig. 2, black dashed line). Note also that L_X and T_X are the lowest of the three models $E0^{250}$, $EO7^{250}_{VD}$ and $EO7^{250}_{IS}$. The cold mass accreted at the centre is now much smaller ($\simeq 2.9 \times 10^3 M_\odot$), while the mass in the cold disc is $\simeq 1.5 \times 10^{10} M_\odot$, and the mass ejected in the galactic wind is $\simeq 1.1 \times 10^{10} M_\odot$. Note that a central black hole in this rotating model would produce a significantly weaker AGN activity than in the $EO7^{250}_{VD}$ model.

Even if the models are structurally quite different from the S0/Sa models in N14, they show a similar ISM evolution, with

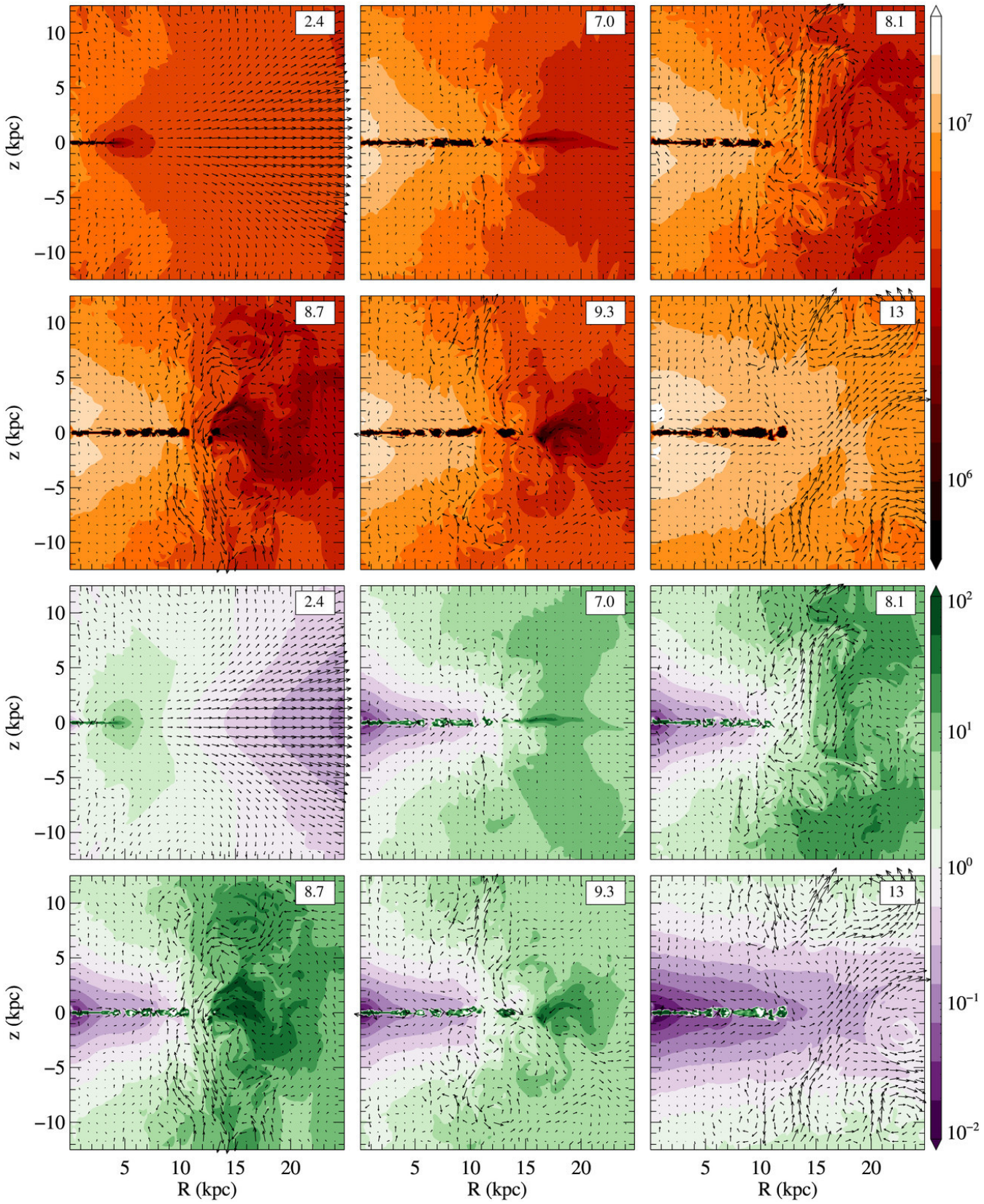

Figure 4. Meridional sections of the temperature in K (six top panels) and heating over cooling time ratio (six bottom panels) for the $EO7^{250}_{IS}$ model of the NFW set, at the times specified in the boxes (in Gyr). Arrows are normalized to the same velocity as in Fig. 1.

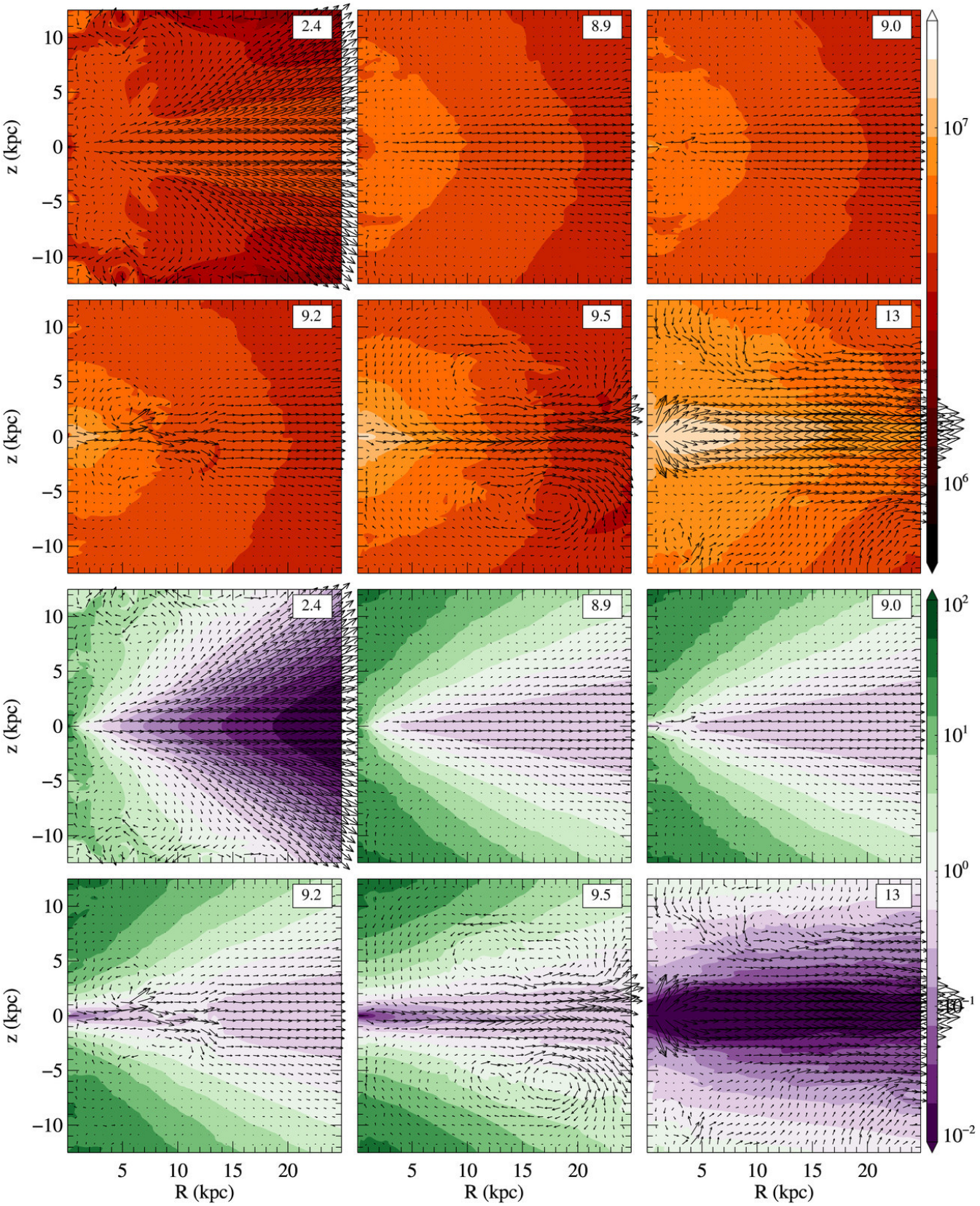

Figure 5. Meridional sections of the temperature in K (six top panels) and heating over cooling time ratio (six bottom panels) for the low mass $EO7^{200}_{VD}$ model of the NFW set, at the times specified in the boxes (in Gyr). Arrows are normalized to the same velocity ad Fig. 1. Note the strong equatorial degassing established at late times.

a lower L_X and T_X in rotating models. However, the number of oscillations in the present set of models is much lower.

3.1.4 The thermalization parameter and an overview of all models

A useful global parameter that helps to quantify the heating of the ISM due to stellar ordered motions is the thermalization parameter γ_{th} (Sec. 2.3, P13, N14). For the $EO7^{250}_{IS}$ galaxy we found that γ_{th} remains at low values ($\simeq 0.08 - 0.28$, see Tables A1 and A2) over the evolution; this means that 1) the ISM almost co-rotates with the stellar population everywhere, and 2) there are not significant ISM velocities in the meridional plane. Note that γ_{th} can attain large values, even larger than unity (see the examples described later in this Section). This happens in general in low-rotation, low-mass systems, where γ_{th} is fully dominated by high velocity galactic winds (see Eq. 14), so that L_m is large even though L_φ remains low. Remarkably enough, also in these high-γ_{th} cases, the azimuthal thermalization parameter $\gamma^{\varphi}_{th} \equiv L_\varphi/L_{rot}$ (Eq. 14) remains low (see Tables A1 and A2), indicating that the ISM rotates almost as fast as the stellar population. One could be tempted to interpret the lack of thermalization of a significant fraction of ordered motions in all the IS models as the reason for the lower T_X of the IS models with respect to their VD counterparts (Fig. 2, black and red dashed lines vs. the solid lines). However, even if this effect certainly contributes, it is not the main reason for the lower T_X in rotating models. Indeed, we found that artificially adding the "missing" thermalization to the equations of hydrodynamics in dedicated test simulations of rotating models leads only to a negligible increase in T_X (see also N14), showing that also other effects contribute to the low T_X (see Sect. 3.3).

We now discuss similarities and differences of the hydrodynamical evolution in galaxy models of different mass (i.e., derived from progenitors with different σ_{e8}). The main features of the family with the spherical progenitor of $\sigma_{e8} = 250$ km s^{-1} are maintained in the $\sigma_{e8} = 300$ km s^{-1} family. In particular, independently of the DM halo profile, increasing σ_{e8}, both L_X and T_X increase. This is expected because more massive models can retain more and hotter gas independently of the flattening and kinematical support. In more massive models the L_X and T_X are less fluctuating with time, the outflow velocities of the galaxy outskirts are lower, and the complicated meridional circulation in the rotating models is reduced (as also found by N14). The final properties of all models are given in Tables A1 and A2. A full discussion of L_X and T_X is given in Sects. 3.2 and 3.3. In general, the ISM temperature, luminosity, radius of the central cooling region, and inflow velocity are directly proportional to σ_{e8}. In massive ($\sigma_{e8} \geq 250$ km s^{-1}) models, at fixed galaxy mass, pure flattening does not affect significantly L_X and T_X, while a major reduction in L_X and T_X is obtained for the isotropic rotators.

The situation is quite different for the families with low mass progenitors ($\sigma_{e8} = 200$ km s^{-1}). These are the only cases where a transition to a global wind can be induced by a change of shape or by rotation, in accordance with the energetic analysis of CP96. This is especially true for the less concentrated Einasto models. In these global wind cases, L_X drops to very low values, due to the very low ISM density, and T_X keeps larger than expected from the trend defined by non-wind models (see Sect. 3.3), due to the reduced cooling, and to thermalization of the meridional motions (see Sects. 3.2 and 3.3 for a detailed discussion). The sensitivity of the flow phase for low-mass models near the transition to the outflow is shown for example by the $EO7^{200}_{VD}$ model with the NFW halo, that experiences two quite distinct evolutionary phases (Fig. 5). At the beginning, a significant equatorial degassing is apparent, coincident with the strong heating in that region. As time increases, the velocity field in the outflow region decreases and gas cooling becomes more and more important outside the V-shaped region around the equator. However, after $\simeq 9$ Gyr, the secular increase of the specific heating, coupled with the shallow potential well, induces again higher and higher velocities. The gas temperature increases again while L_X decreases. The associated $EO7^{200}_{IS}$ model is in a permanent wind phase from the beginning, thus showing the additional effect of rotation in flattened, low-mass galaxies. The differences between the $EO7^{200}_{VD}$ and $EO7^{200}_{IS}$ models are quantified by the associated values of the global quantities at the end of the simulation (see Table A1): $M_{hot} = 0.66 \times 10^9\ M_\odot$ and $0.24 \times 10^9\ M_\odot$ in the VD and IS cases, respectively, where M_{hot} is the ISM mass having $T > 10^6\ K$. Little accretion at the centre is present in the VD but not in the IS, and this shows how different AGN activity may be expected in rotating vs non rotating galaxies, also at low galaxy masses.

3.2 The X-ray ISM luminosity L_X

We now move to describe the properties of L_X for the whole set of galaxy models, as they would be observed at an age of 13 Gyr. The results are summarized in Fig. 6, where the top panels refer to the NFW set and the bottom panels to the Einasto set. L_X is shown versus 3 different galaxy properties, i.e., σ_{e8} (left panels), M_{hot} (central panels), and L_B (right panels). Remarkably, the range of L_X values spanned by the models matches the observed one (see for example the observed $L_X - L_K$ and $L_X - \sigma_{e8}$ trends in Figs. 2 and 5 in Boroson et al. 2011). The most interesting feature of Fig. 6 is the clear L_X difference between flattened rotating models and models of similar σ_{e8} but velocity dispersion supported. As described in the previous Section, the hydrodynamical simulations show that the under-luminosity of rotating galaxies with medium to large σ_{e8} is due to a different flow evolution driven by the presence of angular momentum, which prevents the gas from accumulating in the central regions, leading to the creation of a very hot, low density atmosphere in the centre, and eventually resulting in a lower total L_X. Instead, in VD models the ISM flows directly toward the central galactic regions, where a steep density profile is created. This difference in the hot gas density distribution is a major reason for the systematic difference of L_X (see also Fig. 7). It nicely explains the lower L_X observed for fast rotators than for slow rotators in the ATLAS sample (Sarzi et al. 2013). ETGs with the lowest σ_{e8}, behave differently (see below).

In the central panels of Fig. 6 L_X is plotted against the hot gas content M_{hot}; each rotating model is shifted to the left of the corresponding VD model, thus IS models have also a lower M_{hot} than VD models. This is due to the presence of recurrent cooling episodes driven by rotation, that further contribute to the lowering of L_X. With the exception of the models with the lowest L_B, the systematic differences in M_{hot} are not due to escaping ISM (Fig. 8).

Finally, the right panels of Fig. 6 show how L_X on average increases with the galaxy optical luminosity, however presenting at each L_B a significant spread in L_X, consistent with observations (Boroson et al. 2011). At fixed L_B, round progenitors are found at high L_X, while the dispersion is associated to a mix of flattening and rotation effects. At each L_B, L_X of the VD models is higher than that of IS ones by up to a factor of $\simeq 40$. The largest difference occurs for the more massive and flatter models, and it is much larger than the L_X variation between a spherical progenitor and its most flattened VD version. Indeed, L_X of VD models of identical L_B with different flattening lies in a narrow range, with a weak trend for the

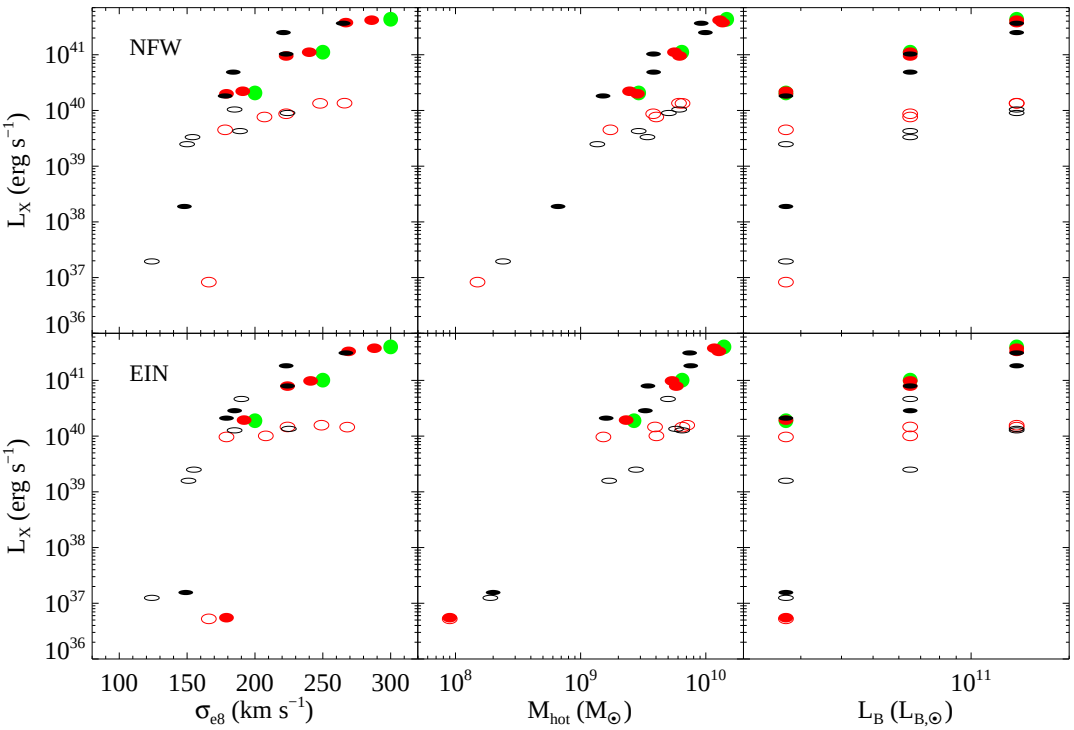

Figure 6. ISM X-ray luminosity L_X in the 0.3–8 keV band at 13 Gyr for all models in the NFW (top panels) and in the Einasto (bottom panels) sets, as a function of σ_{e8}, of the hot ($T > 10^6$ K) ISM mass, and of the galaxy blue optical luminosity; spherical progenitors (green circles) with $\sigma_{e8} = (200, 250, 300)$ have been considered. The green, red and black colours refer to the E0, E4 and E7 models respectively. Filled and empty symbols indicate the fully velocity dispersion supported VD models, and the isotropic rotators IS models, respectively.

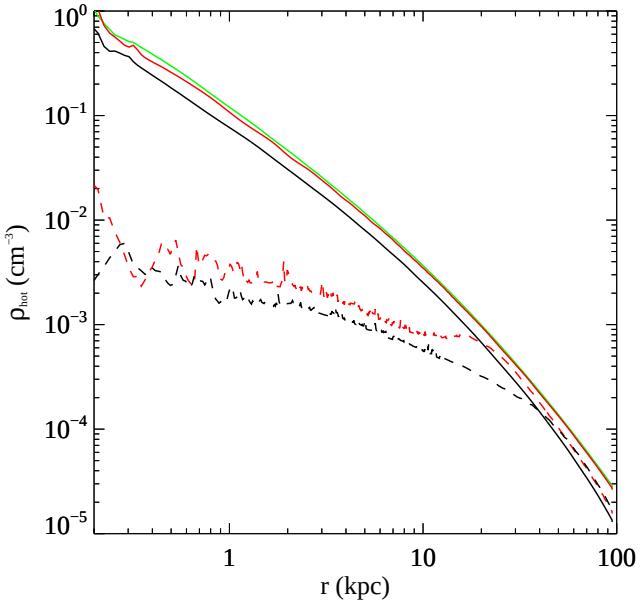

Figure 7. Angle-averaged profile of the hot ISM density at $t = 13$ Gyr for the same models as in Fig. 2. Solid lines refer to VD models, dashed lines refer to IS models.

X-ray luminosity to increase as the galaxy model gets rounder. The same behaviour occurs also among IS models with the same L_B. This indicates that, at fixed L_B and fixed internal kinematics, L_X is only marginally sensitive to even large variations of the flattening degree of the stellar component.

A "zoom" on the specific effects of flattening and rotation is given in Fig. 9, where we plot, separately for each σ_{e8}, and for FO and EO built families, the L_X values of Fig. 6. All models in a given column are characterised by the same optical luminosity. As expected, L_X of FO sub-families spans a narrower range of values than that of the EO cases, due the FO flattening procedure in which the galaxy becomes more concentrated and so outflows are less favoured.

Figure 9 clearly shows how the models with the σ_{e8} = 200 km s^{-1} progenitor behave differently from the rest of the models; this is more evident for the EO flattening, when the galaxy potential well becomes shallower, and thus energetic effects of flattening and rotation are larger than for the FO flattening. For example, the $EO7^{200}_{VD}$ model drops to low L_X, at variance with the $FO7^{200}_{VD}$ model; this drop happens also for the Einasto $EO4^{200}_{VD}$ model. This sharp L_X difference is due to the fact that flattening produces a flow transition to a global wind, in accordance with the CP96 analysis, as described in Sect. 3.1.4. In the NFW case, a further reduction in L_X is attained when introducing rotation in the $EO7^{200}_{IS}$ model, again in accordance with CP96 and P13, where thermalization of ordered motions does not take place. Note how a transition to a very low L_X value is also obtained for the NFW $EO4^{200}_{IS}$ model, just by adding rotation. These findings point out the high sensitivity of the flow phase to (even small) changes in the mass profile (e.g., flattening or mass concentration) and in the stellar kinematics (e.g., rotation) at low galactic masses, for which then it is difficult to predict systematic trends in L_X. We stress that the VD and IS models in each panel are characterized, by construction, by the same gravitational potential, so that the difference in L_X is only due to galactic rotation.

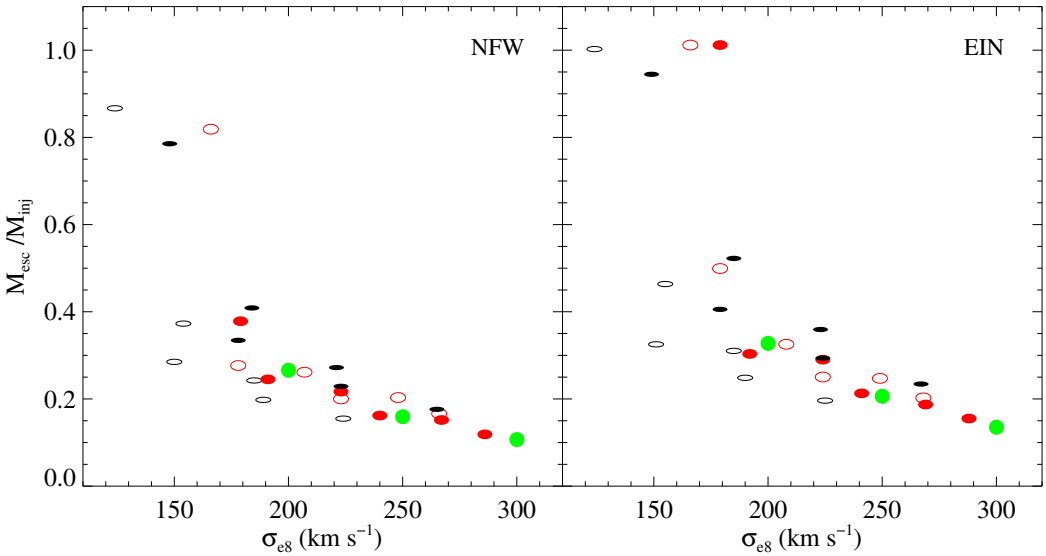

Figure 8. Fraction of escaped ISM mass (M_{esc}) with respect to the total injected mass (M_{inj}, see Tables A1 and A2) at $t = 13$ Gyr, as a function of σ_{e8}, for the whole NFW and Einasto sets. The notation for the symbols is the same as in Fig. 6.

3.3 The X-ray emission weighted temperature T_X

The second important diagnostic explored is the 0.3–8 keV luminosity weighted ISM temperature T_X. The distribution of the T_X values for the whole set of models at the end of the simulations is given in Fig. 10, as a function of σ_{e8}, M_{hot} and L_B.

In general T_X increases with σ_{e8}, a natural consequence of the deeper potential well associated with larger σ_{e8}. This leads to faster stellar (random and ordered) velocities, with the consequent larger energy input from thermalization of the stellar motions. In addition, in a deeper potential the hot gas is retained at a larger T_X. The temperature range spanned by the models agrees well with that of real ETGs, and the observed trend of T_X with σ_{e8} is reproduced (e.g., see Fig. 6 in Boroson et al. 2011, who measured T_X of the pure gaseous component for a sample of 30 ETGs). At high σ_{e8}, the observed T_X values span a narrower range than in our models, likely because the models include very flat and highly rotating ETGs that are missing in the observed sample. Interestingly, instead, the low-σ_{e8} end of the observed $T_X - \sigma_{e8}$ relation shows an increase of dispersion in the T_X values, and a hint for a flattening of the relation with respect to the trend shown at larger σ_{e8}. These features are shown also by our models: at low σ_{e8} the trend of T_X flattens for NFW models, and the scatter around it increases considerably for the Einasto models. This is explained as the temperature counterpart of the L_X behaviour at low σ_{e8} in Fig. 6: the transition to global winds in flattened and rotating low-mass galaxies leads to a reduction in L_X and an increase of T_X with respect to the trend defined by more massive ETGs, or ETGs of similar mass but not in wind. The change in the relationship is due to the thermalization of the resulting meridional flows (while the thermalization of galaxy rotation remains negligible), and to the lower cooling (see Sect. 3.1.4). For example, the $EO4^{200}_{VD}$ and $EO4^{200}_{IS}$ models in the Einasto set, have high T_X as a consequence of the transition to the wind phase.

The middle panels of Fig. 10 show the T_X distribution as a function of M_{hot}. In the NFW set, there is a sequence of T_X values clearly visible at $M_{hot} > 2\times10^9 M_\odot$, with VD models hotter than the corresponding IS models. However, the three models with the smallest amount of hot ISM ($M_{hot} < 10^9 M_\odot$) have higher temperatures than one would expect extrapolating the T_X sequence to very low values of M_{hot}, as a consequence of the transition to the wind phase. A change in the trend is even more visible in the low mass Einasto models, where the stronger tendency to establish a global wind leads to an *increase* of T_X at very low M_{hot}, reaching values even higher than in VD models with large X-ray haloes. In conclusion, at medium-high σ_{e8}, T_X of VD models tends to remain above that of rotating models; at low σ_{e8}, in addition to the cooler branch of rotating models, another hotter branch of IS and VD models appears, made by models in wind.

Finally, the right panels of Fig. 10 show again how T_X of IS models is systematically lower with respect to that of VD ones of same L_B, with the exception of those in the wind phase. As for L_X, T_X of VD models is dominated by the dense central luminous regions. In IS models, instead, the central region is hotter than in VD models, but it is also at a lower density, so that its contribution to T_X is marginal, and T_X is more affected by colder ($T \simeq 2\times10^6$ K) gas located in the outer regions. Thus, the main reason of the lower T_X in IS models of medium-high mass is not galaxy shape, but the importance of galaxy rotation, that drives the hydrodynamical evolution (Sect. 3.1.3). From the Jeans equations, the more a galaxy is flat, the more it can be rotating; thus the E7 IS models are cooler than their VD counterparts, and by a larger amount than for the analogous E4 pair, due to the stronger rotation in the E7 models.

The trend of L_X with T_X for all models is shown in the lower panels of Fig. 11. Also in this figure the models behaviour is strikingly similar to that observed in the Boroson et al. (2011) sample, where a narrow correlation at high $T_X \gtrsim 0.5$ keV is broken into an almost vertical band of L_X values spanning a large range (from 10^{38} to few 10^{41} erg s^{-1}) for kT covering a small range (from 0.2 to 0.5 keV). This trend in the models is explained as the product of the effects described above, resulting in a high sensitivity of the flow phase to small variations in the galaxy structure at the lowest galaxy masses, that on average also have $T_X < 0.5$ keV.

In analogy with Fig. 9, in Fig. 12 we show the distribution of T_X of all models, as a function of σ_{e8} and of the flattening procedure. The additional symbols (crosses) represent T_σ (see Eq. 18), thus they give the temperatures associated with the thermalization of all stellar velocities for VD models (solid crosses), and only to the random

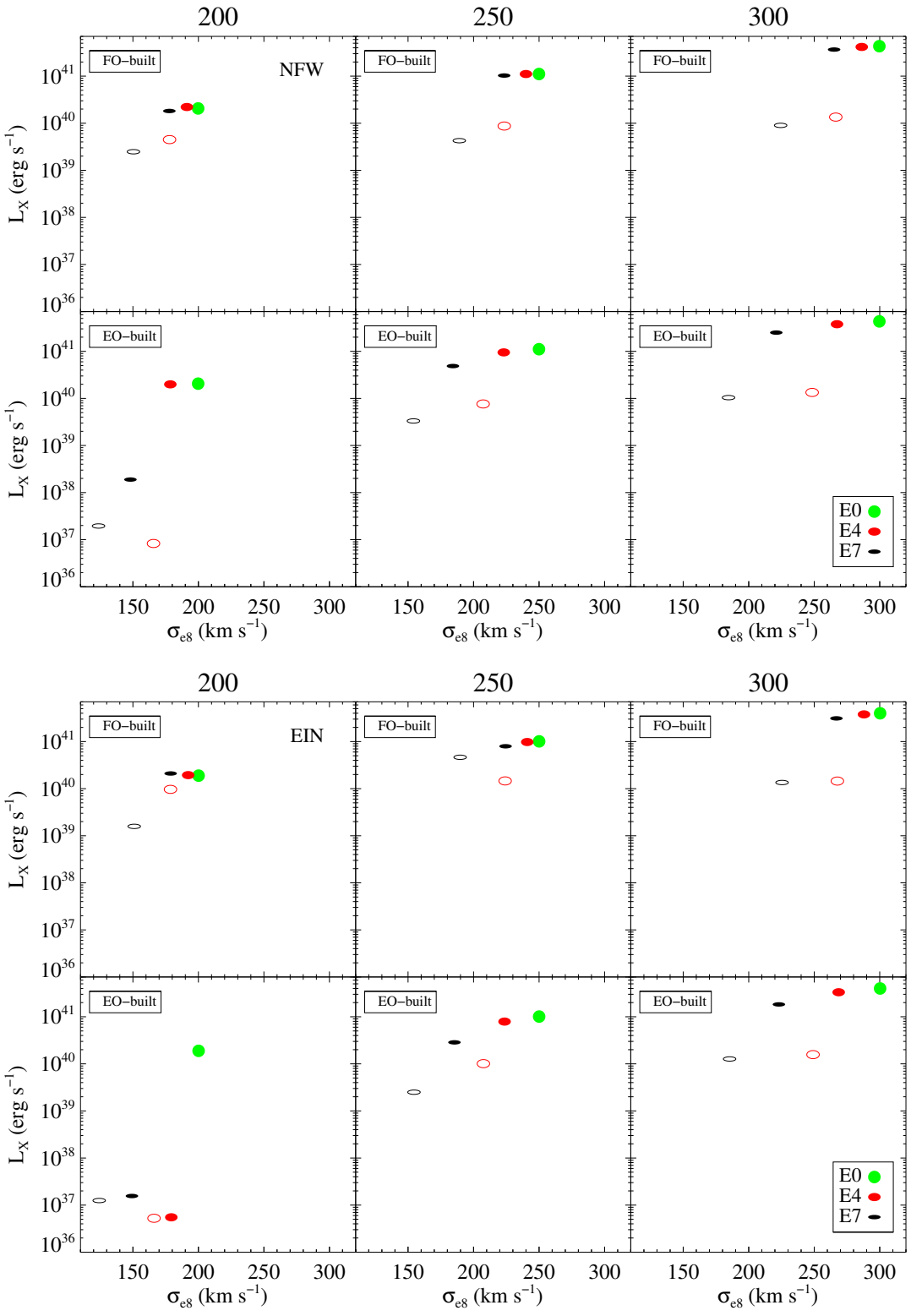

Figure 9. ISM X-ray luminosity L_X in the 0.3–8 keV band at 13 Gyr for the models in the NFW (top six panels) and in the Einasto (bottom six panels) sets as a function of σ_{e8}. Different columns show the results for the families obtained from the spherical progenitors with σ_{e8} = (200, 250, 300) km s^{-1}, and refer to model flattened according to the edge-on or face-on procedure.

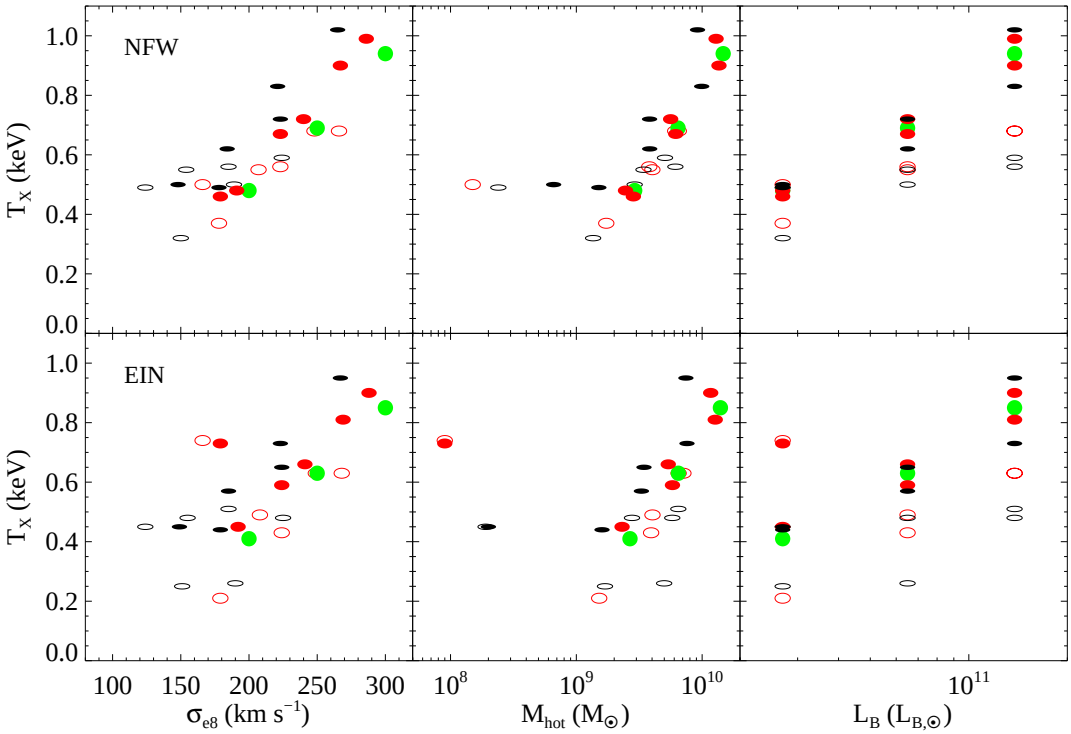

Figure 10. ISM emission weighted temperature T_X in the 0.3–8 keV band at 13 Gyr for all the models in the NFW (top panels) and in the Einasto (bottom panels) sets as a function of σ_{e8}, of the hot ($T > 10^6$ K) ISM mass, and of the galaxy blue optical luminosity. Symbols and colours are as in Fig. 6.

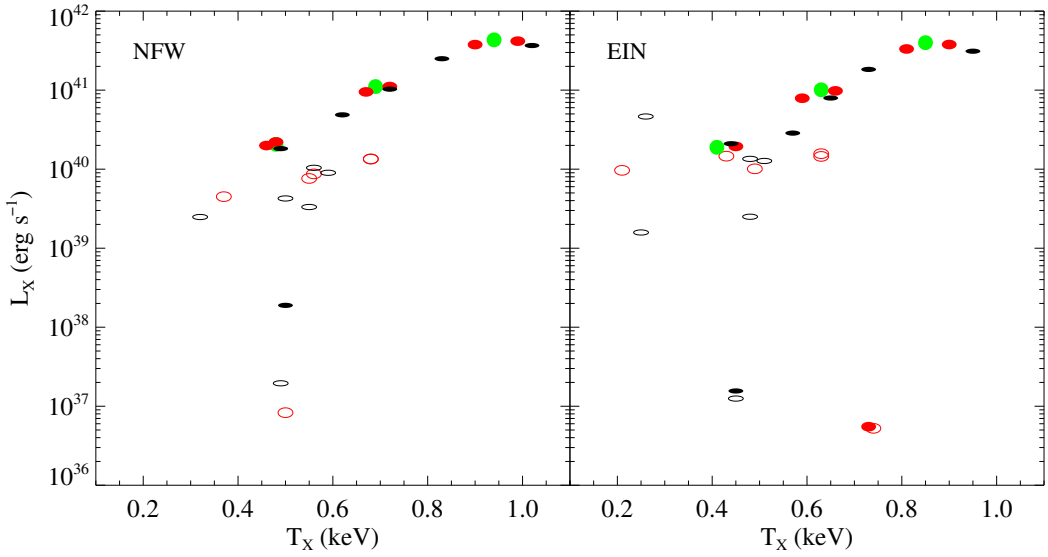

Figure 11. X-ray luminosity L_X with respect to X-ray luminosity weighted temperature T_X at $t = 13$ Gyr for the whole NFW and Einasto sets. The notation for the symbols is the same as in Fig. 6.

part of the stellar velocities for IS models (empty crosses). The values of T_σ depend only on the galaxy structure, and do not contain contributions from gas cooling and SNIa heating. The simulations show that the values of T_{kin} (Eq. 19) are almost coincident with those of T_σ in the medium-high σ_{e8} models (i.e., models in a slow inflow where γ_{th} is very small, see Tables A1 and A2). The low-σ_{e8} wind models, instead, have $T_{kin} > T_\sigma$, and the temperature difference is due to thermalization of the strong meridional motions developed in the wind phase ($T_{kin} \simeq T_\sigma + T_m$, while T_φ remains very small). In Fig. 12 it is even more apparent than in Fig. 10 how VD models are in general hotter than their rotating counterparts, due to the above discussed hydrodynamical effects. In addition, the T_X difference between VD and IS models increases with galaxy flattening, and it is larger for the more massive and FO-built models, and decreases for smaller and EO-built models. Exceptions are found in the low-σ_{e8} EO-built models, as a consequence of the transition to global wind induced by flattening and rotation.

Two interesting considerations can be made by comparing T_X

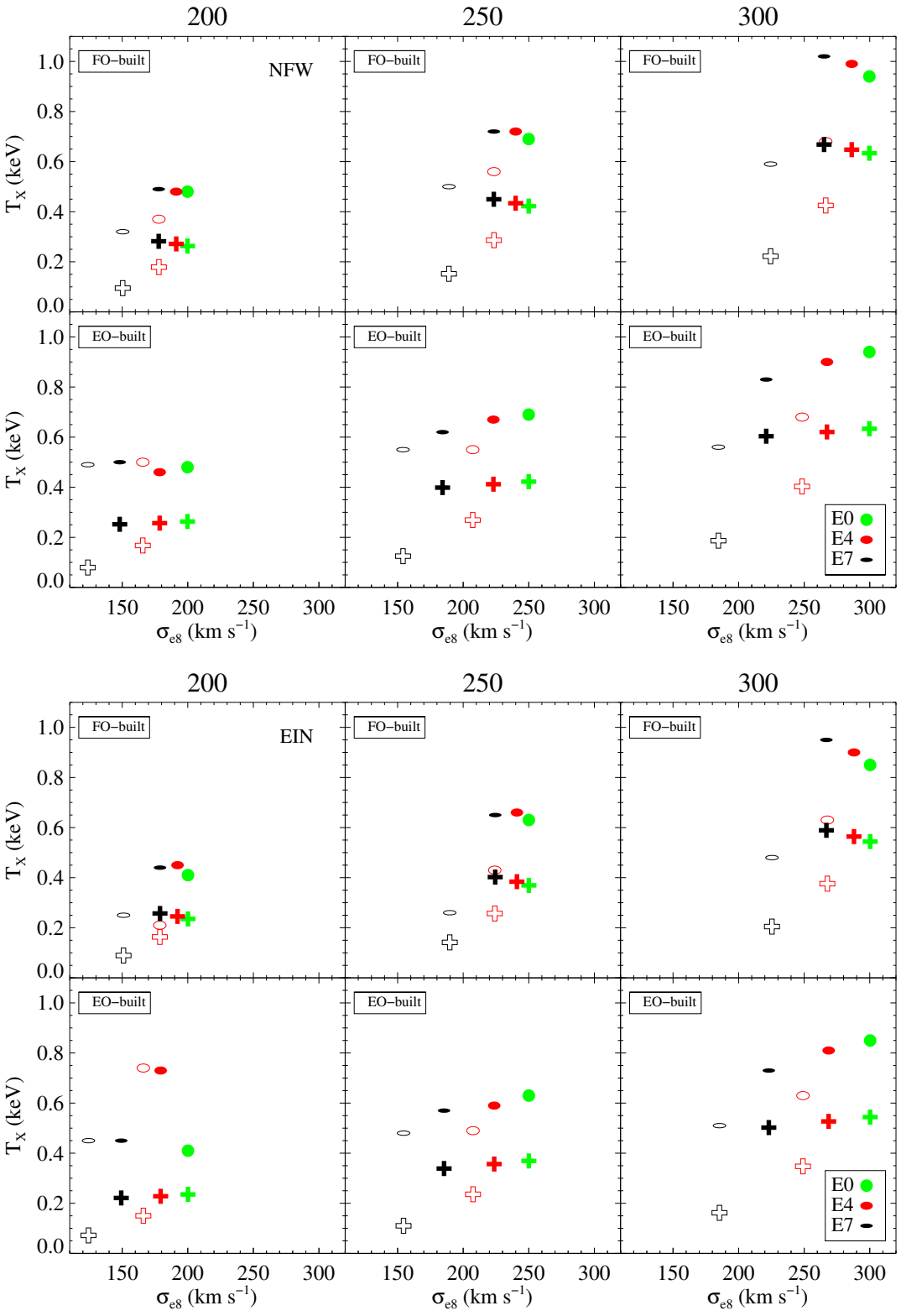

Figure 12. The emission weighted ISM temperature T_X in the 0.3–8 keV band at 13 Gyr for the models in the NFW (top six panels) and in the Einasto (bottom six panels) sets as a function of σ_{e8}. Different columns show the results for the families obtained from the spherical progenitors with σ_{e8} = (200, 250, 300) km/s, and refer to model flattened according to the edge-on or face-on procedure. The green, red and black colours refer to the E0, E4 and E7 models respectively (progenitors are in green). Filled symbols indicate the fully velocity dispersion supported VD models, while empty symbols indicate the isotropic rotators IS models. Crosses show the values of T_σ calculated according to Eq. (18). For the relation of T_σ with T_{kin} and T_X, see the Sect. 2.3.

resulting from the simulations with the temperatures $T_{\rm kin}$ and T_σ associated with the thermalization of stellar motions. The first is that $T_{\rm X}$ of all models is higher than $T_{\rm kin}$ and T_σ, as somewhat expected due to the additional heating contributions (e.g., from SNIa) to the gas, and to the relatively small radiative losses (we recall that $T_{\rm X}$ is computed from the hot, low-density gas only). The second consideration is that, notwithstanding the missing SNIa heating and cooling terms in T_σ, the *trend* of $T_{\rm X}$ with galaxy flattening and rotation is the same as that of T_σ for all models, with the exception of the global wind, low-$\sigma_{\rm e8}$ models. Thus T_σ, except for wind cases, is a good proxy for $T_{\rm kin}$, and a robust indicator of the trend of $T_{\rm X}$ with galaxy properties (shape and internal kinematics). As a final comment, we note that, in general, at fixed $\sigma_{\rm e8}$, Einasto models tend to be slightly colder than the NFW models, both in $T_{\rm X}$ and T_σ, due to the different dark matter profile.

4 DISCUSSION AND CONCLUSIONS

In this paper, in a follow-up of a series of preliminary studies, we performed a large suite of high-resolution 2D hydrodynamical simulations, to study the effects of galaxy shape and stellar kinematics on the evolution of the X-ray emitting gaseous haloes of ETGs. Realistic galaxy models are built with a Jeans code, that allows for a full generality in the choice of axisymmetric galaxy shape and of the stellar and dark matter profiles, that can be tailored to reproduce observational constraints. The dynamical structure of the models obeys the implicit assumption of a 2-integrals phase-space distribution function. Stellar motions in the azimuthal direction are split among velocity dispersion and ordered rotation by using the Satoh (1980) decomposition. In particular, we explored two extreme kinematical configurations, the fully velocity dispersion supported system (VD) and the isotropic rotator (IS), in order to encompass all the possible behaviours occurring in nature. Of course, the VD configuration applies only to a minor fraction of the flat galaxy population (e.g., Emsellem et al. 2011). Moreover, IS models approximate only to some extent the dynamical structure of flat and fast rotating galaxies, since the latter are more generally characterized by a varying degree of anisotropy in the meridional plane with intrinsic flattening (Cappellari et al. 2007). The source of gas is provided by secular evolution of the stellar population (stellar winds from ageing stars and SNIa ejecta). Heating terms account for SNIa events and thermalization of stellar motions.

The main focus of this work is the explanation of long-standing and more recently observed trends of $L_{\rm X}$ and $T_{\rm X}$ with galaxy shape and rotation (as well as, of course, with fundamental galaxy properties as stellar velocity dispersion and optical luminosity). Evidences from previous exploratory theoretical (CP96, P13) and numerical works (DC98, N14) seem to point toward a cooperation of flattening and rotation in establishing the final X-ray luminosity and temperature of the ISM. However which of the two is the driving parameter, and what is the involved physical *mechanism*, had not been clarified yet. From the present investigation, we conclude that more than one physical effect is at play, and that the relative importance of flattening and rotation changes as a function of galaxy mass. We summarize the results discussing first the X-ray luminosity and then the emission-weighted ISM temperature.

1) In low mass galaxy models with a progenitor hosting a global wind, the effects of flattening and rotation are just to make the wind stronger, and all systems are found at the lowest values of $L_{\rm X}$.

2) In case of galaxies energetically near to the onset of a galactic wind, i.e., for ETGs with $\sigma_{\rm e8} \approx 200\,{\rm km\,s^{-1}}$, flattening and rotation contribute significantly to induce a wind, in agreement with the energetic expectations discussed in CP96, with the consequent sharp decrease of $L_{\rm X}$. The transition to a global wind is favoured respectively by the facts that flattening can reduce the depth of the potential well, and that in rotating systems the ISM and the stellar component almost corotate; this reduces (in absolute value) the effective potential experienced by the ISM.

3) In models with $\sigma_{\rm e8} > 200\,{\rm km\,s^{-1}}$, galaxy shape variations, in absence of rotation, have only a minor impact on the values of $L_{\rm X}$, in the sense that fully velocity dispersion supported flattened models have $L_{\rm X}$ similar to or just lower than that of their spherical progenitors.

4) In flat galaxies with $\sigma_{\rm e8} > 200\,{\rm km\,s^{-1}}$, rotation reduces significantly $L_{\rm X}$. Not only the thermalization parameter is low and part of the heating due to stellar motions is missing with respect to the corresponding VD model, but rotation acts also on the hydrodynamics of the gas flow: conservation of angular momentum of the ISM injected at large radii favours gas cooling through the formation of rotating discs of cold gas, reducing the amount of hot gas in the central regions and then $L_{\rm X}$. The effects of angular momentum are clearly visible in Fig. 13, where we show the edge-on projected X-ray surface brightness maps. In conclusion, galaxy flattening has an important, though *indirect* effect for medium-to-high mass galaxies, in the sense that only flattened systems can host significant rotation of the stellar component.

5) The luminosity evolution and the luminosity values at the end of the simulations are similar for the NFW or Einasto dark matter haloes (at fixed stellar structure and similar values of the dark matter halo mass).

The main results concerning the emission-weighted temperature $T_{\rm X}$ can be summarized as follows:

6) As for $L_{\rm X}$, also for $T_{\rm X}$ the response to a variation of shape and internal kinematics is different for low and high mass galaxies. $T_{\rm X}$ does not change appreciably adding flattening and rotation to low mass progenitors that are in the global wind phase. Due to their low density and high meridional velocities, global winds are generally hotter than what expected by extrapolation of the $T_{\rm X}$ of more massive systems. As described at point 2) above, adding flattening and rotation to ETGs energetically near to host a global wind leads to a transition to a wind phase, with the consequent increase of $T_{\rm X}$.

7) In the medium-high mass galaxies a change of shape produces small changes in $T_{\rm X}$. Adding rotation, instead, results in a much lower $T_{\rm X}$. This is because angular momentum conservation leads to the formation of a massive centrifugally supported cold disc and to a lower density of the hot ISM in the central regions above and below the equatorial plane, with respect to VD models. Then, the external, and colder, regions weight more in the computation of $T_{\rm X}$.

8) Overall, for medium-high mass galaxies, $T_{\rm X}$ increases with galaxy mass, independently of the specific dark matter halo profile. In general, in the Einasto haloes the hot gas is systematically cooler and with a larger scatter in $T_{\rm X}$, than in the NFW dark matter haloes of comparable mass.

9) In rotating models the ISM almost corotates with the stars, and so there is a corresponding reduction of the thermalization of the galaxy streaming velocity. At the same time the rotating ISM is less bound, due to the centrifugal support. With the exception of low mass galaxies in the wind phase, T_σ (the temperature associated with the thermalization of the stellar velocity dispersion) is a good proxy for $T_{\rm kin}$, the true thermalization temperature of stellar motions, as

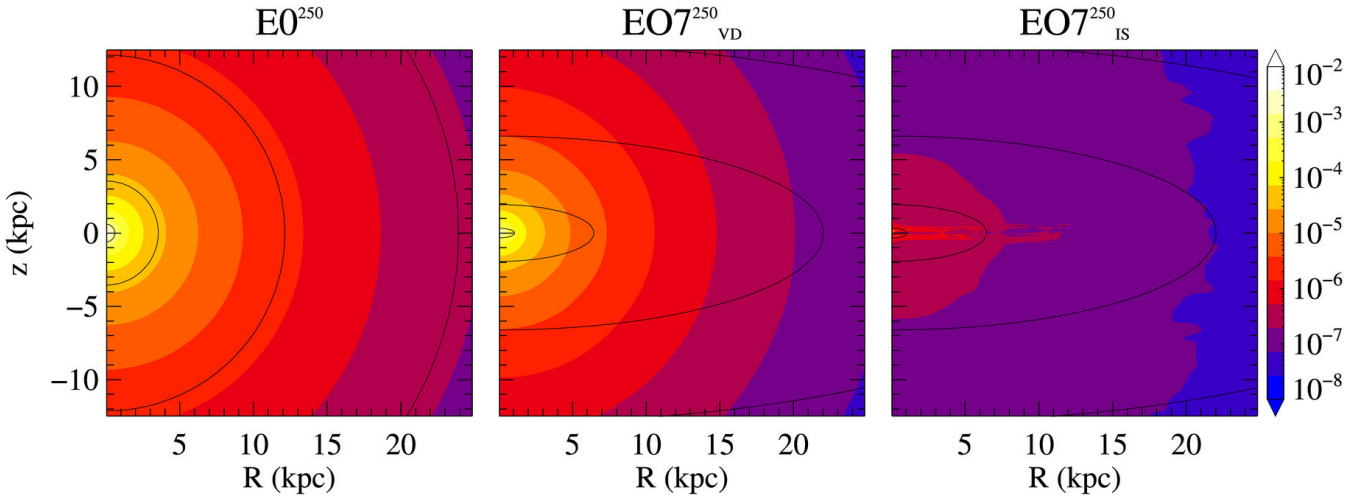

Figure 13. Edge-on 0.3–8 keV surface brightness of the ISM (Σ_X) at 13 Gyr, for $E0^{250}$, $EO7^{250}_{VD}$ and $EO7^{250}_{IS}$ models, respectively; the brightness values on the colour-bar are given in erg s^{-1} cm^{-2}. Superimposed are the isophotes ($\Sigma_\star$) obtained by projecting the galaxy stellar density distribution, with the innermost contour corresponding to 10^4 $M_\odot$ pc^{-2}, and decreasing by a factor of ten on each subsequent contour going outwards. Note that the Σ_X map of the $EO7^{250}_{VD}$ model shows a round shape and a luminous core very similar to the $E0^{250}$ map, whereas $EO7^{250}_{IS}$ map presents a boxy shape and a low-luminosity core.

computed from the simulations; for wind models instead $T_{kin} > T_\sigma$. In general $T_X > T_{kin}$, but the qualitative dependence of T_X on galaxy mass and shape in no wind galaxies is very well reproduced by that of T_σ, a quantity that can be computed without resorting to numerical simulations.

A few important physical phenomena are still missing from the simulations. First, it is obvious that in rotationally supported models the massive and rotating cold discs are natural places for star formation. For observational studies it would be interesting to estimate age and mass of the new stars. From the point of view of the present investigation, the formation of stars, by reducing the amount of cold gas in the equatorial plane, could in principle also modify the evolution of the ISM. We performed a few tests where we activated star formation at a rate $\dot\rho_*$, following Ciotti & Ostriker (2012) and references therein:

$$\dot\rho_* = \eta\frac{\rho}{t_{form}}, \qquad t_{form} = \max(t_{cool}, t_{dyn}), \tag{20}$$

where $0.01 \leqslant \eta \leqslant 0.1$, $t_{cool} = E/\mathscr{L}$ (Eq. 9), and $t_{dyn} \propto 1/\sqrt{G\rho}$. In the test simulations for the model $FO7^{300}_{IS}$ of the NFW set, star formation peaks at the first 3−4 Gyr with a rate of $\approx 10\ M_\odot$ yr^{-1}, and the final mass in the new stellar disc is of the order of few $\times 10^{10}\ M_\odot$; most of the gas disc is consumed by star formation. No significant effects are produced on the ISM luminosity and temperature, so that from this point of view the present results can be considered robust. However, in the test simulations star formation was activated in a "passive" fashion, i.e., only gas subtraction from the computational domain was considered, so that the injection of mass, momentum, and energy due to the evolution of the new stars was not included; these effects will be considered in a future work. An interesting link between our finding of an ubiquitous formation of a cold disc in rotating systems and observed galaxy properties is given by the fact that, among ETGs, it is only in fast rotators that some degree of star formation is observed (Davis et al. 2011; Young et al. 2011; Sarzi et al. 2013).

A second aspect missing here is the self-gravity of the gaseous cold disc. It is expected that self-gravity acts not only to promote star formation, but also to develop non axisymmetric instabilities, that lead to non-conservation of angular momentum of the gas. Phenomenologically, the effects of self-gravity can be viewed as a "gravitational viscosity" (e.g. Bertin & Lodato 2001), that favours accretion of cold gas toward the centre. Such a gas flow toward the centre is of great importance for feedback effects from a central massive black hole in rotating galaxies (Novak et al. 2011; Gan et al. 2014). In a complementary exploration, we are currently studying the interplay between the ISM of a rotating galaxy on large scale and the feedback effects from the central black hole.

ACKNOWLEDGEMENTS

We thank the anonymous referee for constructive comments. L.C. acknowledges Giuseppe Bertin, Jerry and Eve Ostriker, and James Stone for useful discussions. L.C. and S.P. were supported by the MIUR grant PRIN 2010-2011, project 'The Chemical and Dynamical Evolution of the Milky Way and Local Group Galaxies', prot. 2010LY5N2T.

References

Behroozi P. S., Wechsler R. H., Conroy C., 2013, ApJ, 770, 57
Bertin G., Lodato G., 2001, A&A, 370, 342
Boroson B., Kim D.-W., Fabbiano G., 2011, ApJ, 729, 12
Brighenti F., Mathews W. G., 1996, ApJ, 470, 747
Cappellari M. et al., 2007, MNRAS, 379, 418
Ciotti L., Ostriker J. P., 2012, in Astrophysics and Space Science Library, Vol. 378, Astrophysics and Space Science Library, Kim D.-W., Pellegrini S., eds., p. 83
Ciotti L., Pellegrini S., 1996, MNRAS, 279, 240 (CP96)
Davis T. A. et al., 2011, MNRAS, 417, 882
de Vaucouleurs G., 1948, Annales d'Astrophysique, 11, 247
D'Ercole A., Ciotti L., 1998, ApJ, 494, 535 (DC98)
Desroches L.-B., Quataert E., Ma C.-P., West A. A., 2007, MNRAS, 377, 402
Einasto J., 1965, Trudy Astrofizicheskogo Instituta Alma-Ata, 5, 87
Emsellem E. et al., 2011, MNRAS, 414, 888

Eskridge P. B., Fabbiano G., Kim D.-W., 1995, ApJS, 97, 141
Fabbiano G., 1989, ARA&A, 27, 87
Gan Z., Yuan F., Ostriker J. P., Ciotti L., Novak G. S., 2014, ArXiv e-prints
Kim D.-W., Pellegrini S., 2012, Hot Interstellar Matter in Elliptical Galaxies, Astrophysics and Space Science Library, Vol. 378. Springer
Li J.-T., Wang Q. D., Li Z., Chen Y., 2011, ApJ, 737, 41
Maraston C., 2005, MNRAS, 362, 799
Mathews W. G., Brighenti F., 2003, ARA&A, 41, 191
Mellier Y., Mathez G., 1987, A&A, 175, 1
Navarro J. F., Frenk C. S., White S. D. M., 1997, ApJ, 490, 493
Negri A., Ciotti L., Pellegrini S., 2014, MNRAS, 439, 823 (N14)
Novak G. S., Ostriker J. P., Ciotti L., 2011, ApJ, 737, 26
O'Sullivan E., Forbes D. A., Ponman T. J., 2001, MNRAS, 324, 420
Parriott J. R., Bregman J. N., 2008, ApJ, 681, 1215
Pellegrini S., 1999, A&A, 351, 487
Pellegrini S., 2011, ApJ, 738, 57
Pellegrini S., 2012, in Hot Interstellar Matter in Elliptical Galaxies, Astrophysics and Space Science Library, Vol. 378, pp. 21–54, Kim, D.–W. and Pellegrini, S., eds
Pellegrini S., Held E. V., Ciotti L., 1997, MNRAS, 288, 1
Posacki S., Pellegrini S., Ciotti L., 2013, MNRAS, 433, 2259 (P13)
Retana-Montenegro E., van Hese E., Gentile G., Baes M., Frutos-Alfaro F., 2012, A&A, 540, A70
Sarzi M. et al., 2013, MNRAS, 432, 1845
Sarzi M. et al., 2010, MNRAS, 402, 2187
Satoh C., 1980, PASJ, 32, 41
Sazonov S. Y., Ostriker J. P., Ciotti L., Sunyaev R. A., 2005, MNRAS, 358, 168
Smith R. K., Brickhouse N. S., Liedahl D. A., Raymond J. C., 2001, ApJ, 556, L91
Young L. M. et al., 2011, MNRAS, 414, 940

APPENDIX A: TABLES

Table A1. Simulations results for the NFW set at t = 13 Gyr.

name	$M_{\rm inj}$	$M_{\rm esc}$	$M_{\rm gas}$	$M_{\rm hot}$	$L_{\rm X}$	$T_{\rm X}$	$L_{\rm SN}$	$T_{\rm kin}$	T_σ	$T_{\rm v}$	$T_{\rm m}$	$\gamma_{\rm th}$	$\gamma^\varphi_{\rm th}$
	($10^9 M_\odot$)	($10^9 M_\odot$)	($10^9 M_\odot$)	($10^9 M_\odot$)	(10^{40} erg s^{-1})	(keV)	(10^{40} erg s^{-1})	(keV)	(keV)	(keV)	(keV)		
(1)	(2)	(3)	(4)	(5)	(6)	(7)	(8)	(9)	(10)	(11)	(12)	(13)	(14)
$E0^{200}$	12.0	3.2	8.9	2.91	2.06	0.48	10.2	0.26	0.26	1.7E-3	1.7E-3	–	–
$EO4^{200}_{IS}$	11.9	9.8	2.4	0.15	8.29E-4	0.50	10.2	0.40	0.17	0.24	0.21	2.62	0.25
$EO4^{200}_{VD}$	11.9	4.5	7.5	2.84	1.99	0.46	10.2	0.26	0.26	1.5E-3	1.5E-3	–	–
$EO7^{200}_{IS}$	11.9	10.3	1.8	0.24	1.95E-3	0.49	10.2	0.29	0.08	0.22	0.18	1.24	0.22
$EO7^{200}_{VD}$	11.9	9.4	2.8	0.66	1.89E-2	0.50	10.2	0.33	0.25	7.8E-2	7.8E-2	–	–
$FO4^{200}_{IS}$	12.0	3.3	8.8	1.73	0.45	0.37	10.3	0.21	0.18	2.9E-2	9.0E-3	0.31	0.21
$FO4^{200}_{VD}$	12.0	2.9	9.2	2.46	2.21	0.48	10.3	0.27	0.27	3.7E-3	3.7E-3	–	–
$FO7^{200}_{IS}$	12.0	3.4	8.7	1.36	0.25	0.32	10.2	0.12	0.09	2.9E-2	1.1E-2	0.15	0.10
$FO7^{200}_{VD}$	12.0	4.0	8.1	1.51	1.82	0.49	10.2	0.28	0.28	2.0E-3	2.0E-3	–	–
$E0^{250}$	32.2	5.1	27.5	6.43	11.1	0.69	24.3	0.42	0.42	1.2E-3	1.2E-3	–	–
$EO4^{250}_{IS}$	31.7	8.3	23.8	4.02	0.76	0.55	23.9	0.29	0.27	1.8E-2	3.1E-3	0.13	0.10
$EO4^{250}_{VD}$	31.7	6.9	25.2	6.17	9.50	0.67	23.9	0.42	0.41	1.5E-3	1.5E-3	–	–
$EO7^{250}_{IS}$	30.6	11.4	19.7	3.42	0.33	0.55	23.1	0.18	0.13	5.5E-2	4.9E-3	0.20	0.18
$EO7^{250}_{VD}$	30.6	12.5	18.7	3.83	4.87	0.62	23.1	0.41	0.40	1.8E-3	1.8E-3	–	–
$FO4^{250}_{IS}$	32.2	6.5	26.2	3.80	0.87	0.56	24.3	0.30	0.29	1.9E-2	3.9E-3	0.13	0.10
$FO4^{250}_{VD}$	32.2	5.2	27.4	5.62	11.1	0.72	24.3	0.43	0.43	1.6E-3	1.6E-3	–	–
$FO7^{250}_{IS}$	32.2	6.4	26.0	2.91	0.43	0.50	24.2	0.19	0.15	3.7E-2	7.9E-3	0.13	0.10
$FO7^{250}_{VD}$	32.2	7.4	25.3	3.82	10.3	0.72	24.2	0.45	0.45	1.7E-3	1.7E-3	–	–
$E0^{300}$	71.3	7.6	64.7	14.70	43.3	0.94	49.1	0.65	0.65	1.0E-3	1.0E-3	–	–
$EO4^{300}_{IS}$	69.4	14.1	56.0	6.52	1.34	0.68	47.7	0.43	0.42	1.5E-2	1.9E-3	0.07	0.06
$EO4^{300}_{VD}$	69.4	10.5	59.9	13.61	37.7	0.90	47.7	0.63	0.63	1.2E-3	1.2E-3	–	–
$EO7^{300}_{IS}$	65.5	15.9	50.2	6.13	1.04	0.56	45.0	0.23	0.20	2.3E-2	1.5E-3	0.06	0.05
$EO7^{300}_{VD}$	65.5	17.8	48.8	9.92	25.0	0.83	45.0	0.62	0.62	1.2E-3	1.2E-3	–	–
$FO4^{300}_{IS}$	71.8	11.9	60.9	6.11	1.35	0.68	49.4	0.45	0.43	1.7E-2	4.0E-3	0.08	0.06
$FO4^{300}_{VD}$	71.8	8.5	64.3	12.91	41.7	0.99	49.4	0.65	0.65	1.5E-3	1.5E-3	–	–
$FO7^{300}_{IS}$	71.9	11.1	61.8	5.07	0.90	0.59	49.5	0.25	0.23	2.7E-2	4.0E-3	0.06	0.05
$FO7^{300}_{VD}$	71.9	12.7	60.4	9.19	36.7	1.02	49.5	0.67	0.67	1.6E-3	1.6E-3	–	–

Notes: (1) Name of the model. (2) – (3) Total ISM mass injected into and escaped from the numerical grid, respectively. Differences in $M_{\rm inj}$ for models of same $L_{\rm B}$ are accounted for different sampling of ρ_* over the numerical grid. (4) Total ISM mass retained within the galaxy at the end of the simulation. (5) – (7) ISM mass with $T > 10^6$ K, ISM X-ray luminosity in the 0.3–8 keV band, and ISM X-ray emission weighted temperature in the same band, at the end of the simulation. (8) SNIa heating rate at the end of the simulation. (9) – (12) Thermalization temperatures of stellar motions at the end of the simulation, defined accordingly to Eqs. (19) and (18). By construction, $T_{\rm kin} = T_\sigma + T_{\rm v}$; for rotating models $T_{\rm v} = \gamma_{\rm th} T_{\rm rot}$ and $T_\varphi = T_{\rm v} - T_{\rm m} = \gamma^\varphi_{\rm th} T_{\rm rot}$, while for velocity dispersion supported models $T_{\rm v} = T_{\rm m}$ (see Sect. 2.3). (13) – (14) Thermalization parameter as defined in Eq. (15), and its azimuthal component $\gamma^\varphi_{\rm th} = L_\varphi / L_{\rm rot}$ (see Eq. 14), at the end of the simulation.

Table A2. Simulations results for the Einasto set at $t = 13$ Gyr.

name	$M_{\rm inj}$	$M_{\rm esc}$	$M_{\rm gas}$	$M_{\rm hot}$	$L_{\rm X}$	$T_{\rm X}$	$L_{\rm SN}$	$T_{\rm kin}$	T_σ	$T_{\rm v}$	$T_{\rm m}$	$\gamma_{\rm th}$	$\gamma_{\rm th}^{\varphi}$
	$(10^9 M_\odot)$	$(10^9 M_\odot)$	$(10^9 M_\odot)$	$(10^9 M_\odot)$	$(10^{40}$ erg s$^{-1})$	(keV)	$(10^{40}$ erg s$^{-1})$	(keV)	(keV)	(keV)	(keV)		
(1)	(2)	(3)	(4)	(5)	(6)	(7)	(8)	(9)	(10)	(11)	(12)	(13)	(14)
$E0^{200}$	12.0	3.9	8.2	2.67	1.89	0.41	10.2	0.24	0.24	3.7E-3	3.7E-3	–	–
$EO4^{200}_{IS}$	11.9	12.1	0.1	0.09	5.25E-4	0.74	10.2	0.49	0.15	0.34	0.31	4.34	0.28
$EO4^{200}_{VD}$	11.9	12.1	0.1	0.09	5.51-4	0.73	10.2	0.54	0.23	0.31	0.31	–	–
$EO7^{200}_{IS}$	11.9	12.0	0.2	0.19	1.25E-3	0.45	10.2	0.34	0.07	0.27	0.24	1.79	0.14
$EO7^{200}_{VD}$	11.9	11.3	0.9	0.20	1.56E-3	0.45	10.2	0.42	0.22	0.20	0.20	–	–
$FO4^{200}_{IS}$	12.0	6.0	5.7	1.52	0.97	0.21	10.3	0.21	0.16	5.2E-2	2.1E-2	0.63	0.37
$FO4^{200}_{VD}$	12.0	3.6	8.5	2.31	1.94	0.45	10.3	0.25	0.25	2.1E-3	2.1E-3	–	–
$FO7^{200}_{IS}$	12.0	3.9	8.2	1.69	0.16	0.25	10.2	0.14	0.09	4.8E-2	3.0E-2	0.28	0.11
$FO7^{200}_{VD}$	12.0	4.9	7.3	1.60	2.10	0.44	10.2	0.26	0.26	2.8E-3	2.8E-3	–	–
$E0^{250}$	32.2	6.6	26.0	6.47	10.1	0.63	24.3	0.37	0.37	1.4E-3	1.4E-3	–	–
$EO4^{250}_{IS}$	31.7	10.3	21.8	4.03	1.01	0.49	23.9	0.26	0.24	1.8E-2	3.4E-3	0.15	0.12
$EO4^{250}_{VD}$	31.7	9.2	22.9	5.81	7.90	0.59	23.9	0.36	0.36	1.9E-3	1.9E-3	–	–
$EO7^{250}_{IS}$	30.6	14.2	16.9	2.77	0.25	0.48	23.1	0.18	0.11	6.2E-2	9.4E-3	0.27	0.26
$EO7^{250}_{VD}$	30.6	16.0	15.2	3.29	2.86	0.57	23.1	0.35	0.34	3.2E-3	3.2E-3	–	–
$FO4^{250}_{IS}$	32.2	8.1	24.5	3.93	1.46	0.43	24.3	0.27	0.26	1.7E-2	3.8E-3	0.13	0.10
$FO4^{250}_{VD}$	32.2	6.9	25.8	5.38	9.79	0.66	24.3	0.38	0.38	2.0E-3	2.0E-3	–	–
$FO7^{250}_{IS}$	32.2	8.0	24.4	4.99	4.64	0.26	24.2	0.17	0.14	2.9E-2	1.1E-2	0.11	0.07
$FO7^{250}_{VD}$	32.2	9.5	23.3	3.45	7.95	0.65	24.2	0.40	0.40	2.0E-3	2.0E-3	–	–
$E0^{300}$	71.3	9.6	62.7	13.97	39.9	0.85	49.1	0.56	0.56	1.0E-3	1.0E-3	–	–
$EO4^{300}_{IS}$	69.4	17.2	53.2	7.10	1.57	0.63	47.7	0.38	0.36	1.5E-2	1.6E-3	0.09	0.08
$EO4^{300}_{VD}$	69.4	13.0	57.5	12.71	33.2	0.81	47.7	0.54	0.54	1.4E-3	1.4E-3	–	–
$EO7^{300}_{IS}$	65.5	20.3	45.6	6.47	1.27	0.51	45.0	0.20	0.18	2.6E-2	2.2E-3	0.08	0.07
$EO7^{300}_{VD}$	65.5	23.5	43.2	7.58	18.3	0.73	45.0	0.52	0.52	1.8E-3	1.8E-3	–	–
$FO4^{300}_{IS}$	71.8	14.5	58.0	6.50	1.45	0.63	49.4	0.40	0.38	1.8E-2	3.6E-3	0.10	0.08
$FO4^{300}_{VD}$	71.8	11.1	61.8	11.70	37.8	0.90	49.4	0.57	0.57	1.7E-3	1.7E-3	–	–
$FO7^{300}_{IS}$	71.9	14.1	56.6	5.79	1.35	0.48	49.5	0.23	0.21	2.5E-2	3.5E-3	0.07	0.06
$FO7^{300}_{VD}$	71.9	16.9	56.3	7.43	31.1	0.95	49.5	0.60	0.59	1.8E-3	1.8E-3	–	–

Notes: all quantities are as in Table A1.